



# Asymptotic modelling of viscous film flow in slippery flexible tubes

H. Reed Ogrosky o and Mark Schwitzerlett o

<sup>1</sup>Department of Mathematics and Applied Mathematics, Virginia Commonwealth University, Richmond, VA 23220, USA

Corresponding author: Mark Schwitzerlett, msschwitzerl@vcu.edu

(Received 27 December 2024; revised 19 July 2025; accepted 21 August 2025)

An asymptotic model for the flow of a highly viscous film coating the interior of a slippery, flexible tube is developed and studied. The model is valid for the axisymmetric flow of moderately thick films, and accounts for tube flexibility, wall damping, longitudinal tension, slip length and strength of base flow due either to gravity or airflow. In the absence of base flow, linear stability analysis shows the existence of one unstable mode; the presence of base flow allows for multiple unstable modes arising due to the Plateau-Rayleigh instability and elastic instability, with stronger base flow reducing the maximum growth rate. Numerical solutions in the absence of base flow show that slip decreases the amplitude of wall deformations and can significantly decrease the time to plug formation in weakly flexible or strongly damped tubes. For falling films, the impact of model parameters on the critical thickness required for plug formation was analysed by studying turning points in families of travelling-wave solutions; this thickness decreases with slip, flexibility and tension, while damping had a non-monotonic impact on critical thickness. In contrast to model solutions in rigid tubes, for flexible tubes the critical thickness cannot be made arbitrarily large through simply increasing the strength of the base flow. For air-driven films, both slip and flexibility increase the rate of film transport along the tube.

Key words: thin films, lubrication theory

#### 1. Introduction

Highly viscous film flows in tubes arise in several application areas, including human lungs/airways in which airway walls are lined with airway surface liquid (Grotberg & Jensen 2004; Hill *et al.* 2022). The free surface of such film flows in tubes is subject to

several instabilities such as the Plateau–Rayleigh instability (not present in flows along a plane) arising due to surface tension and the curved geometry of a tube (see, e.g. Goren 1962; Yih 1967; Hickox 1971; Joseph *et al.* 1997; Oron, Davis & Bankoff 1997; Craster & Matar 2009). If the tube is flexible, the dynamics can also be driven – under certain conditions – by an elastic instability, or a combination of the two (Halpern & Grotberg 1992; Zhou *et al.* 2016). For moderate-Reynolds-number flows, the Kapitza instability also plays a role in the film flow dynamics; as the focus in this paper will be on low-Reynolds-number flows, the previous two instability mechanisms are in mind here.

The evolution of the film's free surface driven by these instabilities has a number of interesting dynamical outcomes, including chaotic dynamics, travelling-wave trains, wave mergers and interactions and plug formation in which the film pinches off and occludes the tube. The latter can have a significant impact in human airway health for multiple reasons, including the increased wall stresses due to plug formation/rupture that are associated with poor epithelial cell health (Bilek, Dee & Gaver 2003).

Asymptotic modelling studies for films inside tubes go back decades, and have provided insight into these varied dynamical outcomes. A brief and admittedly incomplete review of the most relevant studies is given here now. Hammond (1983) developed a nonlinear model valid for thin films in a rigid tube that explored the evolution of the film's free surface. This approach was extended by Gauglitz & Radke (1988) who employed a long-wave or 'small-slope' approximation that retained a more accurate representation of the film's curvature due to the tube wall; Quevedo Tiznado *et al.* (2018) used a similar method to determine an upper limit for a capillary number that inhibits snap off (plug formation).

A model in a similar vein to that of Hammond (1983) was derived for a falling film by Frenkel (1992); the interactions of free-surface waves in this model were studied numerically by Kerchman & Frenkel (1994), self-similar solutions were found by Kalliadasis & Chang (1994) and plug formation in the model was studied by Jensen (2000). A long-wave model for this set-up was derived and studied by Camassa, Ogrosky & Olander (2014) and Camassa *et al.* (2016) and was shown to have good agreement with low-Reynolds-number experiments. Similarly, for air-driven flow along a tube, Kerchman (1995) developed a model for the film's free surface valid for thin films; this problem was also studied by Camassa *et al.* (2012) who developed long-wave models for the case of films driven by airflow using a simple 'locally Poiseuille' approach to incorporating shear stresses exerted by the air on the film at the free surface. Dietze & Ruyer-Quil (2015), Dietze, Lavalle & Ruyer-Quil (2020), Dietze (2024) developed and studied a weighted residual integral boundary layer model that was found to have good agreement with low-to-moderate-Reynolds-number experiments.

All of the above models were focused on film flows inside rigid tubes. Halpern & Grotberg (1992) extended the modelling work of Hammond (1983) and Gauglitz & Radke (1988) to film flow along a flexible wall in the absence of any base flow. A pair of evolution equations was derived, and it was shown that an elastic instability due to tube flexibility contributed to the overall growth of free-surface disturbances. If the flexibility was great enough, this elastic instability became the dominant driver of the dynamics, leading to 'compliant collapse' of the tube wall. This was further studied by Halpern & Grotberg (1993), in which the impact of insoluble surfactant along the free surface was also included. Zhou *et al.* (2016) studied the flow of a viscoelastic film falling down the inside of a flexible tube, building off of earlier work in a rigid tube with surfactant (Zhou *et al.* 2014). Using an integral boundary layer method, a model was derived valid for moderate Reynolds numbers. Travelling-wave solutions demonstrated the impact of tube flexibility on the free-surface capillary ripples preceding a wave front, and numerical solutions to the evolution equations demonstrated the impact of circumferential tension of the tube

wall on the occurrence of plug formation. Linear stability analysis of viscoelastic film flow with surfactant over a flexible surface was conducted by Patne (2021), who showed the existence of several unstable modes, including a 'solid elastic' mode arising due to shear flow above the film. The focus of the prior modelling studies – and the focus here – is on axisymmetric flow and wall deformation, although it is important to note that non-axisymmetric deformations can play a significant role in the dynamics through buckling in tubes (see, e.g. Heil 1999; Heil, Hazel & Smith 2008; Whang *et al.* 2017).

For flows inside tubes with slip at the wall, Liu & Ding (2017) extended the model of Camassa *et al.* (2014) to include slip at the wall; they documented how slip enhanced growth rates (both temporal and spatio-temporal) – as it also does for film flow along slippery fibres (Haefner *et al.* 2015; Halpern & Wei 2017; Ji *et al.* 2019) – and promoted plug formation through numerical simulations of the model equation. These studies build on previous work demonstrating the impact slip has in promoting instability growth for films along a plane (Samanta *et al.* 2011, 2013; Howell, Robinson & Stone 2013; Hossain & Beherra 2022).

In these asymptotic models, a critical film thickness required for plug formation may be detected by successively repeating numerical simulations of the model equations with a variety of mean film thickness values (e.g. using a bisection method approach), thus narrowing down the thickness region in which the critical thickness lies. In the presence of a base flow, a second way to identify the critical thickness is to study limit points in families of travelling-wave solutions. These limit points serve as a proxy for the critical thickness; through numerical continuation, the impact of model parameters on the critical thickness may be found very efficiently, sweeping across parameter space in a computationally inexpensive way. This method has been used in recent years to study the impact of strength of base flow due to gravity (Camassa *et al.* 2014; Dietze *et al.* 2020), wall heating (Ding *et al.* 2019), insoluble surfactant (Ogrosky, 2021a), airflow (Dietze 2024), wall slip (Schwitzerlett, Ogrosky & Topaloglu 2023) and viscosity ratio in two-layer film flow (Ogrosky, 2021b) on this critical thickness. Information of this kind is essential for development and parameterisation of reduced-order modelling of lungs and airways (Halpern, Jensen & Grotberg 1998; Fujioka *et al.* 2016; Ryans *et al.* 2016).

The goal of the current paper is to build on these previous works and provide new insights into the flow of viscous films inside slippery, flexible tubes, exploring the interplay between tube flexibility and wall slip in enhancing instability growth, film transport and plug formation. A long-wave asymptotic model will be derived for both the case of no base flow and in the presence of base flow due either to gravity or pressure-driven core flow; for the latter case, the 'locally Poiseuille' model of Camassa *et al.* (2012) will be used. Linear stability analysis of the model will be used to identify the impact of model parameters on the growth and speed of small disturbances to the free surface and wall. The nonlinear evolution equations will be solved numerically, and travelling-wave solution families will be found. For falling films, tracing the location of turning points in these families through numerical continuation methods provides an approximate critical thickness required for plugs to form; this thickness will be identified across a variety of parameter values, including strength of base flow, slip length, flexibility, wall damping and wall longitudinal tension. For air-driven films, the impact of parameters on the rate of film transport will be shown.

The current paper is organised as follows. The model is derived – and parameter value ranges discussed – in § 2. Linear stability analysis is conducted in § 3, first for the absence of base flow (§ 3.1), and then with base flow (§ 3.2). Solutions to the evolution equations are found in § 4. Conclusions are given in § 5.

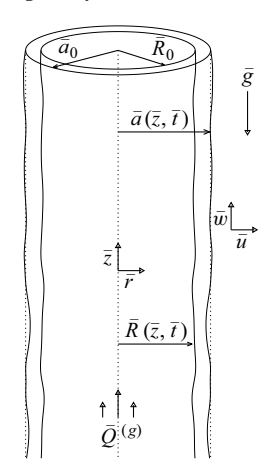


Figure 1. Sketch of the flow configuration and variable definitions.

#### 2. Model derivation

The set-up considered here is an axisymmetric viscous film that lines the interior of a flexible tube. A second, much less viscous fluid (here taken to be air) fills the core region of the tube. Cylindrical coordinates are  $(\bar{r},\bar{z})$  in the radial and axial directions, respectively. The tube wall is taken to have unperturbed radius  $\bar{r}=\bar{a}_0$ , and the free-surface separating the unperturbed core and film sits at  $\bar{r}=\bar{R}_0$ ; see figure 1 for a sketch of the set-up. The free surface will be denoted  $\bar{R}(\bar{z},\bar{t})$  and the tube wall position  $\bar{a}(\bar{z},\bar{t})=\bar{a}_0+\bar{a}_1(\bar{z},\bar{t})$ , where  $\bar{a}_1$  is the perturbation from the undisturbed radius.

Several scenarios will be considered. First, the case where surface tension forces dominate and there is negligible base flow due to gravity or core flow (e.g. in cylindrical capillaries) will be considered. Second, base flow (i) arising in a falling film in a vertical tube, or (ii) due to pressure-driven core flow with volume flux  $\bar{Q}^{(g)}$  will be considered.

# 2.1. Governing equations and boundary conditions

The flow of the fluid is governed by the incompressible, axisymmetric Navier-Stokes equations

$$\bar{\rho}(\bar{u}_{\bar{t}} + \bar{u}\bar{u}_{\bar{r}} + \bar{w}\bar{u}_{\bar{z}}) = -\bar{p}_{\bar{r}} + \bar{\mu} \left[ \frac{1}{\bar{r}} \partial_{\bar{r}}(\bar{r}\bar{u}_{\bar{r}}) + \bar{u}_{\bar{z}\bar{z}} - \frac{\bar{u}}{\bar{r}^2} \right], \tag{2.1a}$$

$$\bar{\rho}(\bar{w}_{\bar{t}} + \bar{u}\bar{w}_{\bar{r}} + \bar{w}\bar{w}_{\bar{z}}) = -\bar{p}_{\bar{z}} + \bar{\mu} \left[ \frac{1}{\bar{r}} \partial_{\bar{r}}(\bar{r}\bar{w}_{\bar{r}}) + \bar{w}_{\bar{z}\bar{z}} \right] - \bar{\rho}\bar{g}, \tag{2.1b}$$

$$\frac{1}{\bar{r}}\partial_{\bar{r}}(\bar{r}\bar{u}) + \bar{w}_{\bar{z}} = 0, \tag{2.1c}$$

where  $(\bar{u}, \bar{w})$  are the velocity components in the  $(\bar{r}, \bar{z})$  directions, respectively, and  $\bar{t}$  is time. Pressure is denoted  $\bar{p}$ ;  $\bar{\mu}$ ,  $\bar{\rho}$  and  $\bar{g}$  denote viscosity, density and acceleration due to gravity, respectively. Letter subscripts denote partial derivatives, and overbars denote dimensional quantities.

At the tube wall  $\bar{r} = \bar{a}(\bar{z}, \bar{I})$ , there is a kinematic boundary condition  $\bar{u} = \bar{a}_{\bar{I}} + \bar{w}\bar{a}_{\bar{z}}$ . Only radial disturbances to the tube will be considered here; thus in the case of no-slip boundary conditions, one would prescribe  $\bar{w} = 0$  and  $\bar{u} = \bar{a}_{\bar{I}}$  at the wall. Here, we explore the impact of slip on the film flow using a Navier slip boundary condition with slip length  $\bar{\Lambda}$ ; due to only radial wall deflection being considered, the resulting boundary conditions at the tube

wall are

$$\bar{w} = -\bar{\Lambda} \; \bar{w}_{\bar{r}}, \tag{2.2a}$$

$$\bar{u} = \bar{a}_{\bar{t}} - \bar{\Lambda} \, \bar{w}_{\bar{r}} \bar{a}_{\bar{r}}. \tag{2.2b}$$

At the free surface,  $\bar{r} = \bar{R}(\bar{z}, \bar{t})$ , there are three boundary conditions: a kinematic boundary condition

$$\bar{u} = \bar{R}_{\bar{t}} + \bar{w}\bar{R}_{\bar{z}}; \tag{2.3}$$

continuity of tangential stress

$$\bar{\mu} \left[ (\bar{w}_{\bar{r}} + \bar{u}_{\bar{z}}) \left( 1 - \bar{R}_{\bar{z}}^2 \right) + 2(\bar{u}_{\bar{r}} - \bar{w}_{\bar{z}}) \bar{R}_{\bar{z}} \right] = \bar{\tau}^{(g)},$$
 (2.4)

with  $\bar{\tau}^{(g)} = \bar{\mu}^{(g)}[(\bar{w}_{\bar{r}}^{(g)} + \bar{u}_{\bar{z}}^{(g)})(1 - \bar{R}_{\bar{z}}^2) + 2(\bar{u}_{\bar{r}}^{(g)} - \bar{w}_{\bar{z}}^{(g)})\bar{R}_{\bar{z}}]$  denoting the tangential stress exerted by the gas flow on the film's free surface; and jump in normal stress (according to the Young–Laplace law)

$$2\bar{\mu}\left(\overline{u}_{\overline{r}} + \overline{w}_{\overline{z}}\overline{R}_{\overline{z}}^{2}\right) + \bar{\mu}\overline{R}_{\overline{z}}\left(\overline{w}_{\overline{r}} + \overline{u}_{\overline{z}}\right) - 2\bar{\mu}^{(g)}\left(\overline{u}_{\overline{r}}^{(g)} + \overline{w}_{\overline{z}}^{(g)}\overline{R}_{\overline{z}}^{2}\right) - \bar{\mu}^{(g)}\overline{R}_{\overline{z}}\left(\overline{w}_{\overline{r}}^{(g)} + \overline{u}_{\overline{z}}^{(g)}\right)$$

$$= \left(\overline{p} - \overline{p}^{(g)}\right)\left(1 + \overline{R}_{\overline{z}}^{2}\right) + \bar{\sigma}\left(1 + \overline{R}_{\overline{z}}^{2}\right)\left(\frac{1}{\overline{R}\left(1 + \overline{R}_{\overline{z}}^{2}\right)^{1/2}} - \frac{\overline{R}_{\overline{z}\overline{z}}}{\left(1 + \overline{R}_{\overline{z}}^{2}\right)^{3/2}}\right), \quad (2.5)$$

with  $\bar{\sigma}$  the surface tension and superscripts of (g) denoting variables in the core gas flow. The tube is assumed to consist of a thin, impermeable wall with density  $\bar{\rho}_w$ , damping coefficient  $\bar{\alpha}$ , circumferential tension  $\bar{T}_{\theta}$ , longitudinal tension  $\bar{T}_{l}$ , thickness  $\bar{h}_{0}$  and dimensionless Poisson ratio  $\gamma$ . Requiring equilibrium of normal forces at the wall yields the equation

$$\bar{\rho}\bar{h}_0\bar{\alpha}\bar{a}_{\bar{t}}\hat{\boldsymbol{r}}_w\cdot\hat{\boldsymbol{n}}_w + \frac{\bar{T}_{\theta}}{\bar{a}}\left(1 + \bar{a}_{\bar{z}}^2\right)^{-\frac{1}{2}} - \bar{T}_{\bar{\ell}}\bar{a}_{\bar{z}\bar{z}}\left(1 + \bar{a}_{\bar{z}}^2\right)^{-\frac{3}{2}} = -\hat{\boldsymbol{n}}_w\cdot\bar{\boldsymbol{T}}\cdot\hat{\boldsymbol{n}}_w, \tag{2.6}$$

with  $\bar{T} = -\bar{p}I + \bar{\mu}(\nabla \bar{u} + \nabla \bar{u}^T)$  and where  $\hat{r}_w$  and  $\hat{n}_w$  are the unit radial and normal vectors at the tube wall. Equation (2.6) may be expressed as the following evolution equation for  $\bar{a}$ :

$$\bar{\rho}_{w}\bar{h}_{0}\bar{\alpha}\bar{a}_{\bar{t}}\left(1+\bar{a}_{\bar{z}}^{2}\right)^{-1/2} + \frac{\bar{T}_{0}}{\bar{a}}\left(1+\bar{a}_{\bar{z}}^{2}\right)^{-1/2} + \frac{\bar{E}\bar{h}_{0}}{1-\gamma^{2}}\frac{\bar{a}-\bar{a}_{0}}{\bar{a}^{2}}\left(1+\bar{a}_{\bar{z}}^{2}\right)^{-1/2} \\ -\bar{T}_{l}\bar{a}_{\bar{z}\bar{z}}\left(1+\bar{a}_{\bar{z}}^{2}\right)^{-3/2} = \bar{p}-\bar{p}_{ext} - \frac{2\bar{\mu}}{1+\bar{a}_{\bar{z}}^{2}}\left[\bar{u}_{\bar{r}}+\bar{w}_{\bar{z}}\bar{a}_{\bar{z}}^{2}-(\bar{u}_{\bar{z}}+\bar{w}_{\bar{r}})\bar{a}_{\bar{z}}\right], \tag{2.7}$$

where we have used the linear version (n=1) of the strain law of Elad, Foux & Kivity (1988; Elad, Kamm & Shapiro 1988) to set the circumferential tension  $\bar{T}_{\theta} = \bar{T}_0 + \bar{E}\bar{h}_0$   $(\bar{a} - \bar{a}_0)/[(1 - \gamma)^2\bar{a}]$  with  $\bar{E}$  the modulus of elasticity (similar to the approach of Halpern & Grotberg (1992)). The first term in (2.7) represents wall damping. The circumferential tension term with coefficient  $\bar{E}\bar{h}_0/(1 - \gamma^2)$  (which will be the primary one retained in what follows) provides a restoring force, acting to return the tube wall to its mean radius  $\bar{a}_0$ . The longitudinal tension term (a diffusion-type term) provides a restoring force in the axial direction. The strength of each of these terms depends on the structural properties of the airways themselves as well as the intrapleural pressure and the surrounding soft parenchymal tissue – which itself exhibits viscoelastic properties – to which the airways are tethered. The magnitude of each of these terms can also be expected

to be a function of airway generation and patient health; while precise values are not known for every airway, it is known that healthy (diseased) airways tend to be more compliant (stiff) and structurally stable (unstable) (Maghsoudi-Ganjeh, Sattari & Eskandari 2021).

There is a steady solution with constant  $\bar{a} = \bar{a}_0$  and  $\bar{R} = \bar{R}_0$  given by

$$\bar{w}_0 = \frac{1}{4} \left( \frac{\bar{p}_{\bar{z}}^{(g)} + \bar{\rho}\bar{g}}{\bar{\mu}} \right) \left( \bar{r}^2 - \bar{a}^2 - 2\bar{R}_0^2 \ln \frac{\bar{r}}{\bar{a}} - \frac{2\bar{\Lambda}}{\bar{a}} (\bar{a}^2 - \bar{R}_0^2) \right) + \bar{R}_0 \bar{\tau}^{(g)} \left( \ln \frac{\bar{r}}{\bar{a}} - \frac{\bar{\Lambda}}{\bar{a}} \right), \tag{2.8a}$$

$$\bar{u}_0 = 0, \qquad \bar{p}_0 = \bar{p}^{(g)} - \frac{\bar{\sigma}}{\bar{R}_0}, \qquad \bar{p}_{ext} = \bar{p}_0 - \frac{\bar{T}_0}{\bar{a}_0}.$$
 (2.8b)

## 2.2. Model derivation

A long-wave asymptotic model for the evolution of the free surface and tube wall will be derived next. Equations (2.1)–(2.7) may be made dimensionless using the following reference scales:

$$r = \frac{\bar{r}}{\bar{R}_0}, \quad z = \frac{\bar{z}}{\bar{\kappa}}, \quad u = \frac{\bar{u}}{\bar{U}_0}, \quad w = \frac{\bar{w}}{\bar{W}_0}, \quad t = \frac{\bar{t}\bar{W}_0}{\bar{\kappa}}, \quad p = \frac{\epsilon\bar{p}\bar{R}_0}{\bar{\mu}\bar{W}_0}, \quad \tau = \frac{\bar{\tau}\bar{R}_0}{\bar{\mu}\bar{W}_0}, \quad (2.9)$$

where  $\bar{k}$  is a typical wavelength of the perturbed free surface,  $\epsilon = \bar{R}_0/\bar{k}$  is an aspect ratio and where  $\bar{W}_0 = \bar{\sigma}/\bar{\mu}$  and  $\bar{U}_0 = \epsilon \bar{W}_0$  are reference velocity scales.

A long-wave approximation,  $\epsilon \ll 1$ , will be employed to develop the model equation. Given that the focus here is on highly viscous films, a further assumption that the Reynolds number  $Re = \bar{\rho} \, \bar{W}_0 \bar{R}_0 / \bar{\mu}$  is  $O(\epsilon)$  will be made. After substituting (2.9) into (2.1) and truncating at  $O(\epsilon)$ , the dimensionless governing equations are given by

$$p_r = 0,$$
  $p_z = \frac{1}{r} \partial_r (rw_r) - Bo,$   $\frac{1}{r} \partial_r (ru) + w_z = 0,$  (2.10)

where  $Bo = \bar{\rho}\bar{g}\,\bar{R}_0^2/\bar{\sigma}$ . At the tube wall, r = a(z, t), the truncated dimensionless boundary conditions are

$$w = -\Lambda w_r, \qquad u = a_t - \Lambda w_r a_z, \tag{2.11}$$

where  $\Lambda = \bar{\Lambda}/\bar{R}_0$ . At the free surface, r = R(z, t), the boundary conditions are

$$u = R_t + wR_z,$$
  $w_r = \tau^{(g)},$   $p - p^{(g)} = -\frac{\epsilon}{R} + \epsilon^3 R_{zz}.$  (2.12)

Note that one term of  $O(\epsilon^3)$  has been included in (2.12). Despite not being strictly valid to retain, this term is commonly kept in film flow models of this type as it has been shown to provide the correct cutoff wavenumber in linear stability analysis and produces growth rates in good agreement with the full governing equations.

The model equation for the dimensionless free surface R(z, t) may be found by integrating the continuity equation from (2.1c) across the fluid layer from R(z, t) to a(z, t) and applying the necessary boundary conditions from (2.11) and (2.12) to produce

$$\frac{1}{2}\frac{\partial}{\partial t}(a^2 - R^2) + \frac{\partial}{\partial z}\int_{R(z,t)}^{a(z,t)} rw \, \mathrm{d}r = 0. \tag{2.13}$$

The velocity profile w may be found by solving the dimensionless w-momentum equation subject to the remaining boundary conditions in (2.11) and (2.12), resulting in

$$w = \frac{1}{4} (p_z + Bo) \left[ r^2 - a^2 - 2R^2 \ln \frac{r}{a} - \frac{2\Lambda}{a} (a^2 - R^2) \right] + R\tau^{(g)} \left( \ln \frac{r}{a} - \frac{\Lambda}{a} \right); \quad (2.14)$$

this is equivalent to (2.15) in Schwitzerlett *et al.* (2023) up to a choice of velocity scales except that here the tube radius a(z, t) is no longer a constant.

There are several ways in which one could incorporate the effects of pressure-driven airflow on the free surface. For small-amplitude disturbances, it is typical to specify a constant shear stress at the free surface; here, in order to study the evolution of disturbances beyond the linear regime, a variable shear stress will be considered. We elect to use what has been referred to in prior studies as a 'locally Poiseuille' approximation in which the airflow – presumed to be much faster than the highly viscous liquid flow – essentially experiences the free surface as a rigid wall. This allows for a decoupled treatment of the airflow in which the free-surface stresses  $p_z^{(g)}$  and  $\tau^{(g)}$  may be estimated and incorporated into (2.14). Briefly, the air is assumed to flow at a constant volume flux  $\bar{Q}^{(g)}$  through the core region (though a constant pressure gradient could also be incorporated). Modelling the (assumed laminar) airflow using Poiseuille flow with the long-wave assumption that the free surface varies slowly in z produces the dimensionless local estimates of the stresses

$$p_z^{(g)} = -\frac{4Ca^{(g)}}{R^4}, \qquad \tau^{(g)} = \frac{2Ca^{(g)}}{R^3},$$
 (2.15)

where  $Ca^{(g)}$  is the capillary number, defined as  $Ca^{(g)} = 2\bar{\mu}^{(g)}\bar{Q}^{(g)}/\pi\bar{R}_0^2\bar{\sigma}$ . Additional details of these calculations can be found in, e.g. Camassa *et al.* (2012) and Schwitzerlett *et al.* (2023). Note that fully coupled dynamics could also be used as in, e.g. Dietze & Ruyer-Quil (2015).

Substituting (2.14) into (2.13) results in the final governing equation for the film's free surface

$$\frac{1}{2}(a^2 - R^2)_t = \left[Ca^{(g)}f_1(R; a) + \frac{1}{16}(Bo R^2 + R_z + R^2 R_{zzz})f_2(R, a)\right]_z, \quad (2.16)$$

where

$$f_1(R;a) = \frac{1}{4R^4} \left[ -a^4 + 2a^2R^2 - R^4 - 4\Lambda a \left( a^2 - R^2 \right) \right],\tag{2.17a}$$

$$f_2(R,a) = \frac{a^4}{R^2} + 3R^2 - 4a^2 + 4R^2 \ln\left(\frac{a}{R}\right) + \frac{4\Lambda}{aR^2} (a^2 - R^2)^2, \tag{2.17b}$$

and where we have returned to the original aspect ratio by rescaling z and t by  $\epsilon$ .

For the tube wall, substitution of (2.9) into (2.7) and truncating at  $O(\epsilon)$  (and again returning to the original aspect ratio) gives

$$\psi a_t = T_l a_{zz} - \frac{1}{\Gamma} \frac{a - a_0}{a^2} + T_0 \frac{a - a_0}{a_0 a} + 1 - \frac{1}{R} + R_{zz}, \tag{2.18}$$

where

$$\psi = \frac{\bar{\rho}_w \bar{h}_0 \bar{\alpha} \bar{R}_0}{\bar{\mu}}, \quad T_0 = \frac{\bar{T}_0}{\bar{\sigma}}, \quad T_l = \frac{\bar{T}_l}{\bar{\sigma}}, \quad \Gamma = \frac{(1 - \gamma^2)\bar{\sigma}}{\bar{E}\bar{h}_0}. \tag{2.19}$$

The parameter  $\psi$  is a damping parameter proportional to the product of the wall-to-fluid mass ratio and damping ratio, and  $\Gamma$  is the ratio of surface tension forces to elastic forces.

# H.R. Ogrosky and M. Schwitzerlett

Both the damping and longitudinal tension terms are of  $O(\epsilon^2)$  (as well as the curvature term  $R_{zz}$ ) but are retained here as in Halpern & Grotberg (1992) and Zhou *et al.* (2016) in order to assess the impacts of flexibility on the film flow dynamics. Also note that the pressure  $p_{ext}$  is assumed to satisfy  $(p - p_{ext})/\epsilon = 1 - (1/R) + R_{zz} + (T_0/a_0)$ .

Equations (2.16) and (2.19) comprise the model. In the case of no base flow ( $Ca^{(g)} = Bo = 0$ ) and no slip ( $\Lambda = 0$ ), the model could be termed a long-wave version of the thin-film model studied by Halpern & Grotberg (1992); we will explore the impact of base flow and slip on both thin and moderately thick films. In the case that  $Ca^{(g)} = \Lambda = 0$ , the problem set-up is a Newtonian version of the problem studied by Zhou *et al.* (2016) (viscoelastic film flow down a flexible tube); their model started from the same equation for tube motion (2.7) but was derived using an integral boundary layer method. In the case of a rigid tube, so that  $a = a_0$  (which could be accomplished by, e.g. taking  $\psi \to \infty$  or  $\Gamma \to 0$ ), the single-partial differential equation model of Schwitzerlett *et al.* (2023) is recovered.

#### 2.3. Parameter values

Here, we briefly discuss the range of parameter values which will be considered. There are a total of fifteen parameters to be specified: eight describing the tube:  $\bar{T}_l$ ,  $\bar{T}_0$ ,  $\bar{E}$ ,  $\bar{\alpha}$ ,  $\bar{\rho}_w$ ,  $\bar{h}_0, \bar{a}_0, \bar{\gamma}$ ; three parameters describing the fluid:  $\bar{\mu}, \bar{\sigma}, \bar{\rho}$ ; two parameters describing the airflow:  $\bar{\mu}^{(g)}$ ,  $\bar{Q}^{(g)}$ ; and two corresponding to the film thickness and boundary condition:  $\bar{R}_0$  and  $\bar{\Lambda}$ , respectively. The final model contains eight dimensionless parameters –  $Ca^{(g)}$ , Bo,  $a_0, \psi, T_0, T_1, \Gamma, \Lambda$  – that govern the film flow; this reduction in number of parameters is not only the result of non-dimensionalisation but also simplifying assumptions (e.g. small Re, 'locally Poiseuille' airflow) and the way in which the original parameters were grouped in the tube wall equation (2.7). Our parameter choices will largely fall in a range roughly corresponding to those considered by Halpern & Grotberg (1992) and Zhou et al. (2016). Parameter values that motivated Halpern & Grotberg (1992) for the tube wall were, e.g.  $\bar{E} = 60\,000\,\mathrm{dyn\,cm^{-2}}$ ,  $\bar{\rho}_w = 1\,\mathrm{g\,cm^{-3}}$ ,  $\bar{T}_l = 25\,\mathrm{dyn\,cm^{-1}}$ ,  $\gamma = 0.5$ ,  $\bar{T}_0 = 0$ dyn/cm,  $\bar{\alpha} = 10 \text{ s}^{-1}$ ,  $\bar{h}_0 = 0.0025 \text{ cm}$ ; for the film, we will take  $\bar{\rho} = 1 \text{ g cm}^{-3}$  and surface tension  $\bar{\sigma} = 20 \text{ dyn cm}^{-1}$ . Similar to Halpern & Grotberg (1992), a range of dimensionless parameter values – which is motivated by the above choices but also recognises the wide variety of tube and fluid properties possible – will be considered:  $I_l \in [0, 1], T_0 = 0$  and  $\Gamma \in [0, 1].$ 

As the focus here is on situations where gravity may play a non-negligible role in the film's evolution, we will consider a range of tube radii and film thicknesses:  $\bar{a}_0 \in [0.025, 0.5]$  cm,  $\bar{R}_0 \in [0.0225, 0.4]$  cm; here the lower bounds correspond to values considered by Halpern & Grotberg (1992) appropriate for the bronchioles in which gravity may be neglected, and the upper end of the range reasonable for upper airways. As the viscosity of mucus is a property that varies widely (especially in the presence of shear stress created by airflow considered here), a wide range of viscosities may be appropriate, e.g.  $\bar{\mu} \in [0.01, 100]$  P. Given these uncertainties, a wide range of dimensionless parameters will be used:  $a_0 \in [1.05, 1.5]$ ,  $Bo \in [0, 10]$ ,  $\psi \in [0, 10^5]$ , although values outside these ranges may be considered briefly in order to make a point about the model solutions.

For the airflow,  $\bar{\mu}^{(g)} = 1.81 \times 10^{-4}$ ; in previous experiments designed to model upper airways, volume fluxes of  $\bar{Q}^{(g)} \in [10\ 1000]\ \text{cm}^3\ \text{s}^{-1}$  were used Kim *et al.* (1986), Camassa *et al.* (2012), Kim, Iglesias & Sackner (1987). For lower airways this value may be expected to be much smaller. In an effort to capture the range of values possible, we will consider  $Ca^{(g)} \in [0, 1]$ . Finally, for slip length, (Brochard-Wyart *et al.* 1994) note that a slip length of  $1-10\ \mu\text{m}$  may be appropriate for silicone oils in experiments like those of Camassa

Parameter	Reference value (§ 3)	Description	
Bo	0	Bond number, $\bar{\rho}\bar{g}\bar{R}_0^2/\bar{\mu}$	
$Ca^{(g)}$	0	Capillary number, $2\bar{\mu}^{(g)}\bar{Q}^{(g)}/\pi \bar{R}_0^2\bar{\sigma}$	
$a_0$	1.1	Film thickness parameter, $\bar{a}_0/\bar{R}_0$	
Λ	0	Slip length, $\bar{\Lambda}/\bar{R}_0$	
$\psi$	2000	Damping parameter, $\bar{\rho}_w \bar{h}_0 \bar{\alpha} \bar{R}_0 / \bar{\mu}$	
Γ	0.5	Tube flexibility parameter, $(1 - \gamma^2)\bar{\sigma}/\bar{E}\bar{h}_0$	
$T_l$	0	Longitudinal tension, $\bar{T}_l/\bar{\sigma}$	
$T_0$	0	Circumferential tension, $\bar{T}_0/\bar{\sigma}$	
χ	0.5	Modified tube flexibility, $\Gamma/(1-\Gamma T_0)$	

Table 1. Reference values used in § 3.

Parameter	Standard values (§ 4.3)	
Во	0.125	
$Ca^{(g)}$	0	
$a_0$	1.15	
Λ	0	
$\psi$	16 000	
$\Gamma$	0.5	
$T_l$	0	
$T_0$	0	

Table 2. Standard case values used in § 4.3.

et al. (2012), leading to values of  $\Lambda$  as high as 0.01; other modelling studies with slip have investigated higher dimensionless slip lengths (e.g. Liu & Ding (2017), who study up to  $\Lambda \approx 0.1$  using the scalings here). We note that apparent wall slip depends not only on fluid and polymer properties but on properties of the tube wall, and that while slip boundary conditions have been found to aid in addressing discrepancies between models and experiments in a wide variety of problems, there is some debate over the validity of their use in some settings (see, e.g. Lauga et al. 2005; Bäumchen & Jacobs 2009; Kavokine, Netz & Bocquet 2021 and references therein). Motivated by these previous studies, we will consider  $\Lambda \in [0, 0.1]$ .

A set of reference parameter values is given in table 1 for § 3, and a second set is given in table 2 for § 4.3.

## 3. Linear stability analysis

Linear stability analysis of the model equations is conducted next. In order to study the evolution of small disturbances to a constant solution, let  $R = 1 + Ae^{i(kz-\omega t)}$  and  $a = a_0 + Be^{i(kz-\omega t)}$ , where it is assumed that  $A \ll 1$  and  $B \ll 1$ . Substituting these into (2.16) and (2.19) produces an eigenvalue problem with a quadratic characteristic equation

$$\tilde{a}(i\omega)^2 + \tilde{b}(i\omega) + \tilde{c} = 0, \tag{3.1}$$

with

$$\tilde{a} = \psi, \tag{3.2a}$$

$$\tilde{b} = a_0 (1 - k^2) - k^2 T_l - \frac{1}{\chi a_0^2} - \psi \left[ \left( C a^{(g)} g_1 + B o g_2 \right) i k + g_5 (k^4 - k^2) \right], \tag{3.2b}$$

$$\tilde{c} = \left[ \left( Ca^{(g)}g_1 + Bo g_2 \right) ik + g_5 \left( k^4 - k^2 \right) \right] \left( k^2 T_l + \frac{1}{\chi a_0^2} \right) + \left[ Ca^{(g)}g_3 + Bo g_4 \right] ik \left( 1 - k^2 \right), \tag{3.2c}$$

where we have adopted the notation of  $\chi = \Gamma/(1 - \Gamma T_0)$  from Halpern & Grotberg (1992) and where

$$g_1 = a_0^4 - a_0^2 + 2\Lambda a_0 (2a_0^2 - 1), \tag{3.3a}$$

$$g_2 = \frac{1}{2} \left( 1 - a_0^2 + 2 \ln a_0 - \frac{2\Lambda}{a_0} (a_0^2 - 1) \right), \tag{3.3b}$$

$$g_3 = -a_0^3 + a_0 - \Lambda(3a_0^2 - 1), \tag{3.3c}$$

$$g_4 = \frac{1}{4} \left( a_0^3 - 2a_0 + \frac{1}{a_0} + \Lambda \left( 3a_0^2 - 2 - \frac{1}{a_0^2} \right) \right), \tag{3.3d}$$

$$g_5 = \frac{1}{16} \left( a_0^4 - 4a_0^2 + 3 + 4 \ln a_0 + \frac{4\Lambda}{a_0} (a_0^2 - 1)^2 \right). \tag{3.3e}$$

Note that the effect of  $T_0$  in the linear stability can thus be incorporated through a modified value of  $\Gamma$ ; as a result (and due to the reference value of  $T_0 = 0$ ), in what follows we set  $\chi = \Gamma$  and focus on how  $\Gamma$  impacts the dynamics.

In the case of an undamped tube, i.e.  $\psi=0$ , (3.1) is linear and has solution  $i\omega=-\tilde{c}/\tilde{b}$ . When  $\psi>0$ , there are two solutions; in the limit of infinite damping, i.e.  $\psi\to\infty$ :  $i\omega=0$ ,  $(Ca^{(g)}g_1+Bo\ g_2)ik+g_5(k^4-k^2)$ , with the second solution corresponding to the rigid tube model growth rate as in Schwitzerlett *et al.* (2023). This rigid tube limit may also be recovered in the limit  $\Gamma\to0$ , achieved by taking  $\bar{E}\to\infty$ , e.g. as noted by Halpern & Grotberg (1992).

## 3.1. No base flow

In the case of no base flow  $(Ca^{(g)} = Bo = 0)$ , the growth rate without damping is

$$i\omega = \left[g_5(k^4 - k^2)(1 + k^2T_l\chi a_0^2)\right] / \left[\chi a_0^3(1 - k^2) - 1 - k^2T_l\chi a_0^2\right]. \tag{3.4}$$

Note that in the rigid tube case ( $\chi = 0$ ) these growth rates are  $i\omega = g_5(k^2 - k^4)$ , leading to the wavenumber of maximum growth rate  $k_{max} = 1/\sqrt{2}$ . In the other extreme, as noted by Halpern & Grotberg (1992), if  $\chi$  is sufficiently large, here  $\chi > 1/a_0^3$ , then there is an infinite growth rate for finite k given by

$$k_{\infty} = \left(1 - \frac{1}{\chi a_0^3}\right) / \left(1 + \frac{T_l}{a_0}\right).$$
 (3.5)

In the case of damping, with  $\psi > 0$ , there are two solutions to (3.1); one of these is unstable for 0 < k < 1, with  $k_c = 1$  the cutoff wavenumber. Note that at k = 0, these solutions are

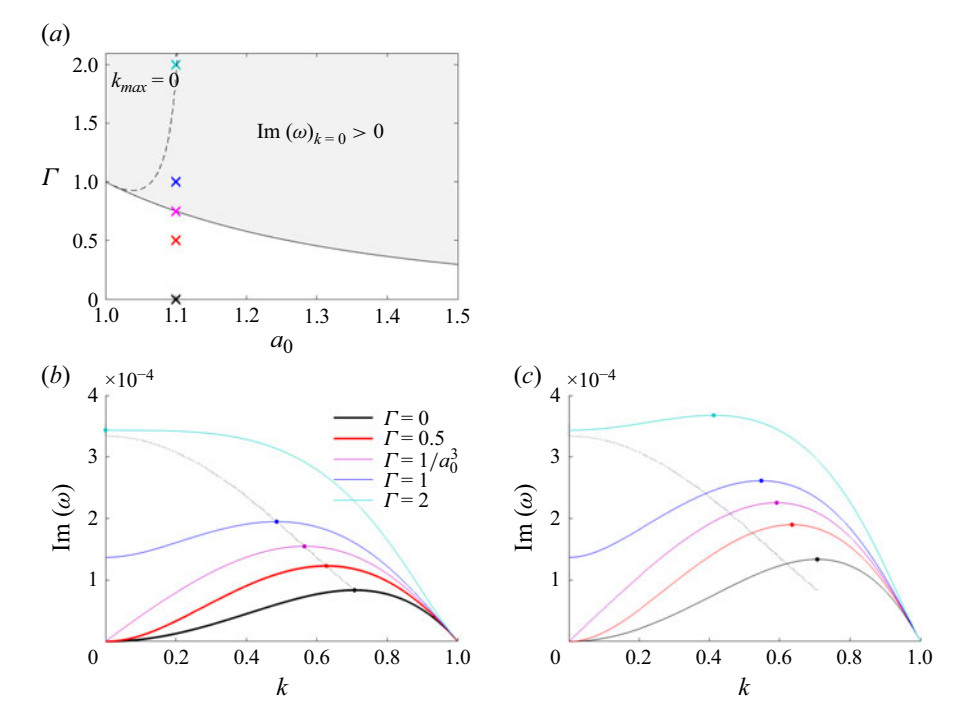


Figure 2. (a) Value of  $\Gamma = 1/a_0^3$  (solid line) and smallest  $\Gamma$  for which  $k_{max} = 0$  (dashed line) as a function of  $a_0$ . The  $\times$  symbols correspond to growth rate plots in (b). (b)–(c) Growth rates for a variety of  $\Gamma$  values; (b)  $\Lambda = 0$ ; (c)  $\Lambda = 0.02$ . Unless otherwise mentioned, parameter values are the reference values in table 1; thick red line denotes reference value growth rates. Thick black line denotes the rigid tube case ( $\Gamma = 0$ ). Dotted black line denotes maximum growth rate with  $\Lambda = 0$  as  $\Gamma$  varies.

$$i\omega = 0, \ \frac{1}{\psi} \left( \frac{1}{\chi a_0^2} - a_0 \right),$$
 (3.6)

so that for  $\chi > 1/a_0^3$  the k = 0 mode is also unstable. This can lead to the 'compliant collapse' scenario observed by Halpern & Grotberg (1992) in simulations of a thin-film model, in which the Plateau–Rayleigh instability becomes subdominant to this wall collapse in driving the dynamics. In their thin-film model,  $\Gamma > 1$  was required for the k = 0 mode to be unstable, although they noted that, in nonlinear simulations, smaller values of  $\Gamma$  were sufficient to trigger this compliant collapse.

Here, film thickness is also seen to lower the value of  $\Gamma$  required for the k=0 mode to be linearly unstable. Figure 2(a) shows the region of  $a_0-\Gamma$  space (i) for which the growth rate at k=0 is positive, and (ii) for which the growth of  $\Gamma$  is largest at k=0, i.e.  $k_{max}=0$ . Figure 2(b) shows the growth rates for  $a_0=1.1$  and several values of  $\Gamma$  corresponding to the  $\times$  symbols in (a). Increasing  $\Gamma$  increases growth rates for all k and decreases the wavenumber of maximum growth rate  $k_{max}$  which eventually reaches 0 for sufficiently large  $\Gamma$ . Note that the curve with  $\Gamma=0$  represents the rigid tube growth rate curve, while the red curve represents the parameter values in table 1.

Figure 2(c) shows growth rates with identical parameters to (b) but with  $\Lambda = 0.02$ . While slip leaves the k = 0 growth rates unchanged, it has the impact of promoting the Plateau–Rayleigh instability, leading to larger values of  $k_{max}$  for all  $\Gamma$  shown here.

How does the magnitude of wall damping parameter  $\psi$  affect the growth rates? Figure 3(a) shows the growth rate curves for various values of  $\psi$ , with  $\Gamma = 0.5$ .

# H.R. Ogrosky and M. Schwitzerlett

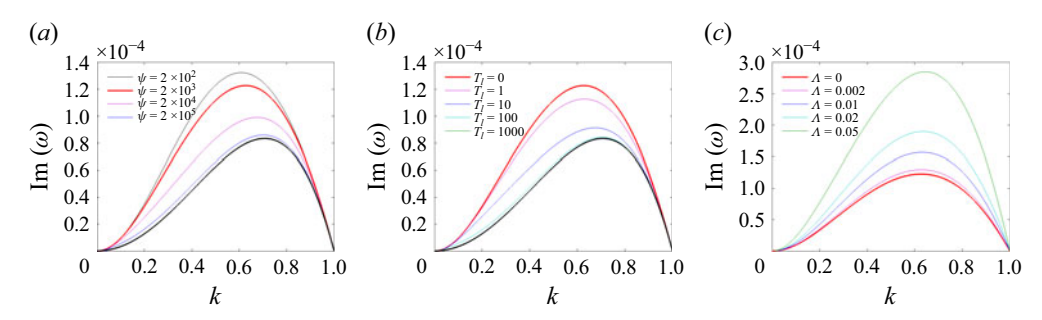


Figure 3. Growth rates for various parameter values. Unless otherwise mentioned, parameter values are the reference values in table 1; thick red lines denote reference value growth rates. Thick black lines denote the rigid tube case ( $\Gamma = 0$ ). Growth rates are shown for various (a)  $\psi$ , (b)  $T_l$  and (c)  $\Lambda$ .

Increasing  $\psi$  decreases the growth rates and increases  $k_{max}$ . In the limit  $\psi \to \infty$ , the growth rates approach those of the rigid tube. In the limit  $\psi \to 0$ , the growth rates approach some curve with reduced  $k_{max}$  and a maximum growth rate roughly 40 % larger than that of the rigid tube case for these parameter values. Note that, if  $\chi > 1/a_0^3$ ,  $k_{max}$  may be again reduced all the way to zero (not shown here). The impact of  $T_l$  is shown in figure 3(b). Increasing  $T_l$  has a similar impact on growth rates as increasing  $\psi$  does, with the rigid tube approached as  $T_l \to \infty$ .

In rigid tubes, slip has been shown previously to increase growth rates in film flow models by allowing liquid to flow more readily into a growing wave, promoting the Plateau–Rayleigh instability (e.g. Halpern & Wei 2017; Liu & Ding 2017), as seen earlier in figure 2(c). This is also the case for fixed  $\Gamma = 0.5$  in figure 3(c), in which increasing the slip length  $\Lambda$  results in increased growth rates without modifying  $k_{max}$ . In the case where  $\Gamma > 1/a_0^3$ , slip does modify  $k_{max}$  (not shown here), with the value of  $k_{max}$  closer to its rigid tube value of  $1/\sqrt{2}$  the larger the values of slip lengths.

# 3.2. Base flow

Next, the impact of base flow, i.e. with either  $Ca^{(g)} > 0$  or Bo > 0, on the linear stability is examined. Note that, in the absence of damping, base flow does not change the growth rates, as positive values for  $Ca^{(g)}$  and Bo only modify the imaginary part of the solution  $i\omega = -\tilde{c}/\tilde{b}$ , creating non-zero phase speed.

Figure 4(a) shows the impact of varying Bo on growth rates in the presence of damping  $(\psi > 0)$  for  $\chi < 1/a_0^3$ . Increasing Bo decreases the maximum growth rates, while increasing growth rates for the smallest values of k. The wavenumber of maximum growth rate  $k_{max}$  increases with increasing Bo.

For  $\chi > 1/a_0^3$ , varying Bo has a more complicated impact on growth rates. As shown in figure 4(b), for sufficiently large Bo, there is a second unstable mode (e.g. Bo = 0.075); if Bo is large enough, these two branches of the growth rate curve meet and pinch off (e.g. Bo = 0.1). Also note that the value of  $k_{max}$  changes abruptly from a value near 0.5 to  $k_{max} = 0$  as Bo increases from 0 to 0.075.

The presence of base flow also introduces a non-zero phase speed, shown in figure 4(c,d), for various values of Bo and  $Ca^{(g)}$ , respectively. In figure 4(c), the phase speed shows dependence on k only for very small k. As expected, increasing Bo results in waves falling down the tube faster. Similarly, as  $Ca^{(g)}$  increases in figure 4(d), the phase speed increases as free-surface waves move up the tube. Again only weak dependence on k is seen.

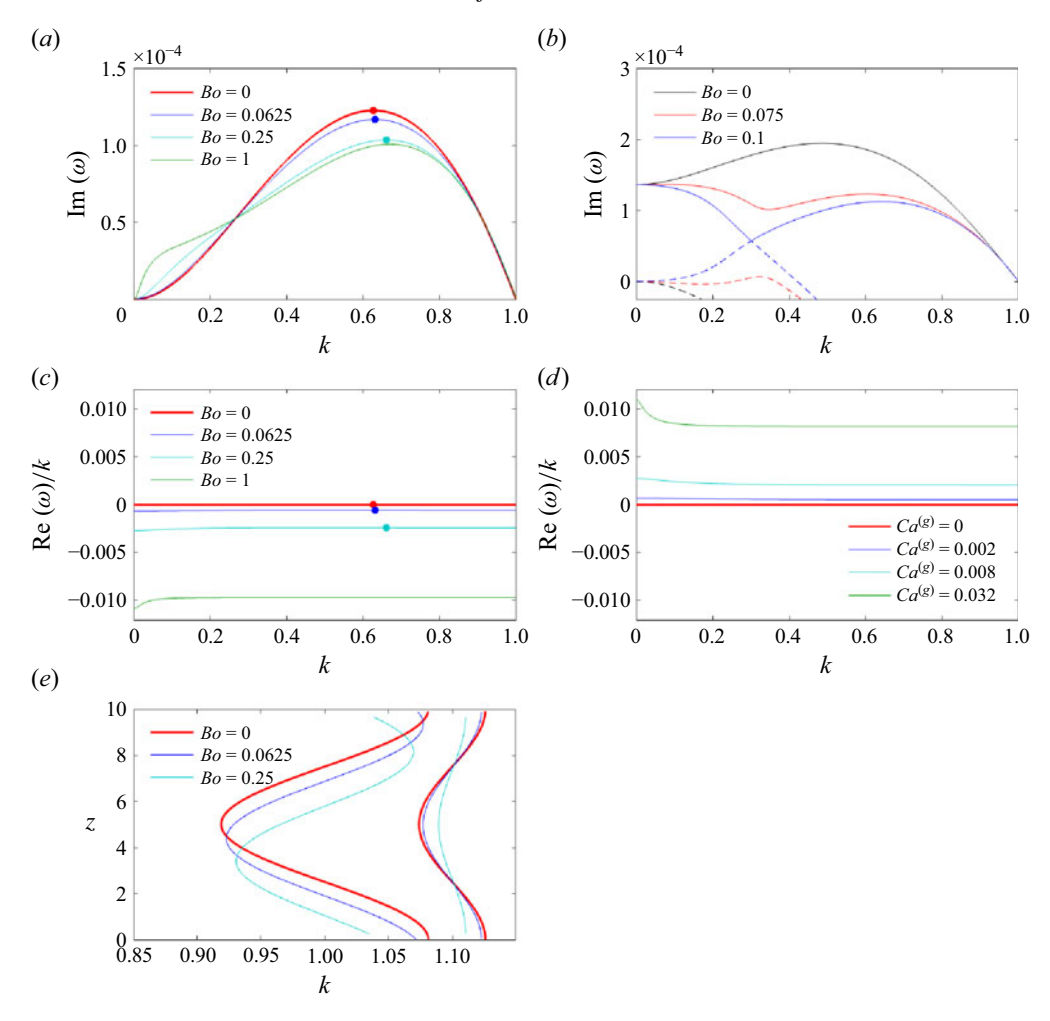


Figure 4. (a)–(b) Growth rates are shown for various Bo: (a)  $\Gamma = 0.5$ ; (b)  $\Gamma = 1$ . (c)–(d) Phase speed for various values of Bo and  $Ca^{(g)}$ ; thick red lines denote speeds with parameter values in table 1. (e) Profile of free surface and wall for k and Bo values corresponding to dots in (a), (c). Note that the magnitude of disturbances is arbitrary, although relative magnitude is meaningful, determined by the eigenvalues and eigenvectors. Unless otherwise mentioned, parameter values are those of table 1.

The profile of the wall and free surface are shown in figure 4(e) for solutions corresponding to the dots in (a), (c). In all cases the disturbance to the free surface is larger than the disturbance to the wall. Increasing Bo slows the growth in the free-surface disturbance and, more noticeably, in the wall disturbance. A phase shift between free surface and wall is introduced by increasing Bo, with the free-surface disturbance leading the wall disturbance.

We close this section by mentioning that increasing the film thickness increases growth rates.

## 4. Solutions to nonlinear equation

Next, we explore solutions to the model equations (2.16) and (2.19). Some details of the numerical methods used are given in § 4.1; solutions in the absence or presence of base flow are given in §§ 4.2 and 4.3, respectively.

#### 4.1. Numerical methods

Equations (2.16) and (2.19) are solved on a domain of length L using periodic boundary conditions. A pseudospectral method was used, in which spatial derivatives were calculated in Fourier space and nonlinearities were calculated in physical space. An explicit second-order predictor–corrector method for time integration was used. As the quantity  $a^2 - R^2$  is a conserved quantity, conservation of film volume was monitored throughout each simulation; when the change in film volume between successive time steps exceeded some chosen threshold (set to be  $10^{-8}$  or smaller in all simulations), the update to the free surface and tube wall were recalculated with the time step decreased by a factor of two. Initial conditions consisted of a constant solution plus a series of small-amplitude perturbations (with random amplitude and phase shift) with varying wavenumber

$$R = 1 + \sum_{k=1}^{N} \tilde{R}_k \cos(2\pi kz/L + c_{1,k}), \quad a = a_0 + \sum_{k=1}^{N} \tilde{a}_k \cos(2\pi kz/L + c_{2,k}).$$
 (4.1)

Travelling-wave solutions were also found by seeking steady solutions in a moving reference frame with speed c, i.e. seeking functions Q(Z) = R(z - ct) and b(Z) = a(z - ct), where Z = z - ct. Substituting this ansatz into the model equations results in a fourth-order ordinary differential equation (ODE) and a second-order ODE. The equation for Q may be integrated once, yielding a third-order equation (with a constant of integration K); the resulting equations are

$$K = \frac{c}{2} (b^2 - Q^2) + Ca^{(g)} f_1(Q, b) + \frac{1}{16} (Bo Q^2 + Q' + Q^2 Q''') f_2(Q, b), \quad (4.2a)$$

$$-c\psi a' = T_l a'' - \frac{1}{\Gamma} \frac{a - a_0}{a^2} + T_0 \frac{a - a_0}{a_0 a} + \left(1 - \frac{1}{Q} + Q''\right). \tag{4.2b}$$

Equation (4.2) were solved by first identifying an equilibrium solution  $Q=Q_0$  and  $b=b_0$ . By varying the wave speed, a Hopf bifurcation in the solution family may be identified. The numerical continuation package XPP/AUTO was used for this task; XPP is a numerical package for analysing dynamical systems (Ermentrout 2002) that provides a convenient way to access AUTO (Doedel *et al.* 2008). Moving onto a branch of periodic solutions from the Hopf bifurcation, families of travelling-wave solutions may be found while varying any model parameter, including period size. The mean value of  $b^2-Q^2$  was held fixed throughout these continuations. Details of this numerical approach can be found in Camassa *et al.* (2016), including the addition (and subsequent removal) of a small viscosity-like term to the model. This aids in finding Hopf bifurcations by avoiding zero-Hopf bifurcations which can be more difficult to identify numerically; this viscosity term was set to zero after moving onto a branch of periodic solutions.

#### 4.2. No base flow

For the case of no base flow, i.e.  $Ca^{(g)} = Bo = 0$ , simulations were first conducted for a period of  $L \approx 2.86\pi$ . This choice for the domain matches that used by Halpern & Grotberg (1992) as linear stability analysis shows it to be the most unstable wave. As has been discussed in previous studies, e.g. Hammond (1983), Halpern & Grotberg (1992), when the film is thinner than some critical thickness, the growth in amplitude of a wave saturates with the free surface approaching some steady-state profile. When the film is thicker than this critical thickness, enough fluid drains into the wave from the surrounding substrate to allow the wave to undergo accelerated growth with  $\min_{z} R \to 0$  in finite time.

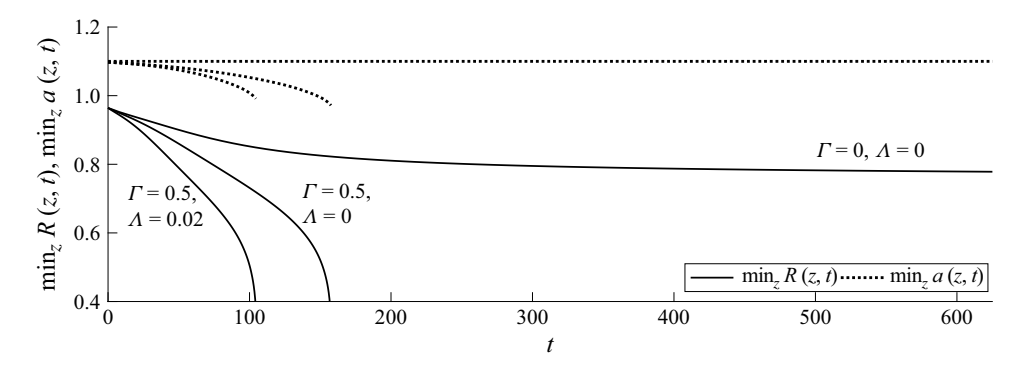


Figure 5. Evolution of  $\min_z R(z, t)$  and  $\min_z a(z, t)$  for three simulations with  $a_0 = 1.1$ ,  $\psi = 16,000$ ,  $Bo = Ca^{(g)} = T_1 = T_0 = 0$ .

Figure 5 shows the values of  $\min_z R(z, t)$  and  $\min_z a(z, t)$  for three simulations; one for a rigid tube ( $\Gamma = 0$ ,  $\Lambda = 0$ ), one for a flexible tube ( $\Gamma = 0.5$ ,  $\Lambda = 0$ ) and one for a flexible tube with slip ( $\Gamma = 0.5$ ,  $\Lambda = 0.02$ ). The beginning stages of this accelerated growth are evident for the flexible tube solutions, while in the rigid tube case the film thickness parameter  $a_0 = 1.1$  is (barely) sufficiently small to prevent the formation of a plug, with  $\min_z R(z, t)$  approaching a constant value.

Snapshots of the free surface are shown for these three simulations in figure 6. In the second case, flexibility enhances the Plateau–Rayleigh instability, resulting in faster growth and the eventual formation of a plug. The inclusion of slip further promotes plug formation, with a plug forming quicker than in the no-slip case. The tube wall deformation is slightly less in the presence of slip.

Figure 7(a) shows the closure time (here approximated as the time needed for min R to reach 0.55) for a variety of  $\Gamma$ ,  $\psi$  and  $\Lambda$  values. The chosen values of  $\psi$  and  $\Gamma$  produce the same phenomenon observed by Halpern & Grotberg (1992) in which the closure time decreases with decreasing  $\Gamma$ ; for large damping ( $\psi = 16\,000$ ), this decrease is particularly pronounced for values of  $\Gamma$  between 0.5 and 1, which corresponds to  $\Gamma$  crossing the  $1/a_0^2$ threshold. The impact of slip is seen as well; for small damping and large  $\Gamma$ , the impact of slip is minimal as flexibility provides the main enhancement to the Plateau–Rayleigh instability, leading to plug formation. For large damping or for small  $\Gamma$  – i.e. for tubes that are 'weakly' flexible – the contribution of slip is more significant. For each value of  $\psi$ , figure 7(c) shows the ratio of closure times found with slip to no-slip. For 'weakly' flexible tubes, slip can cut the closure time by a factor of 4 or more. We note that a threshold value is a common way in thin-film modelling studies to estimate the closure time (see, e.g. Cassidy et al. (1999)) as the model cannot be run all the way to min R = 0 due to the inverse powers and logarithms of R in (2.16). While the chosen threshold value of min R = 0.55 results in a slight underestimate of the closure time, extended simulations run for some cases show that every time min R decreases below 0.55, a plug is formed very soon afterwards.

How does the film thickness parameter affect the closure time? Figure 7(b) shows the closure time for a variety of a values and several combinations of  $\Lambda$  and  $\Gamma$ . It appears that for thin films, closure time is more sensitive to the change in  $\Gamma$  (flexibility), while for thicker films, the closure time is more sensitive to the change in  $\Lambda$  (slip). This is confirmed in figure 7(d), which shows the ratio of each of the three curves with markers in panel (b) (namely rigid tube with slip, flexible tube with slip and flexible tube without slip) to the closure time found for a rigid tube with no slip. In all cases, the greatest drop in closure

# H.R. Ogrosky and M. Schwitzerlett

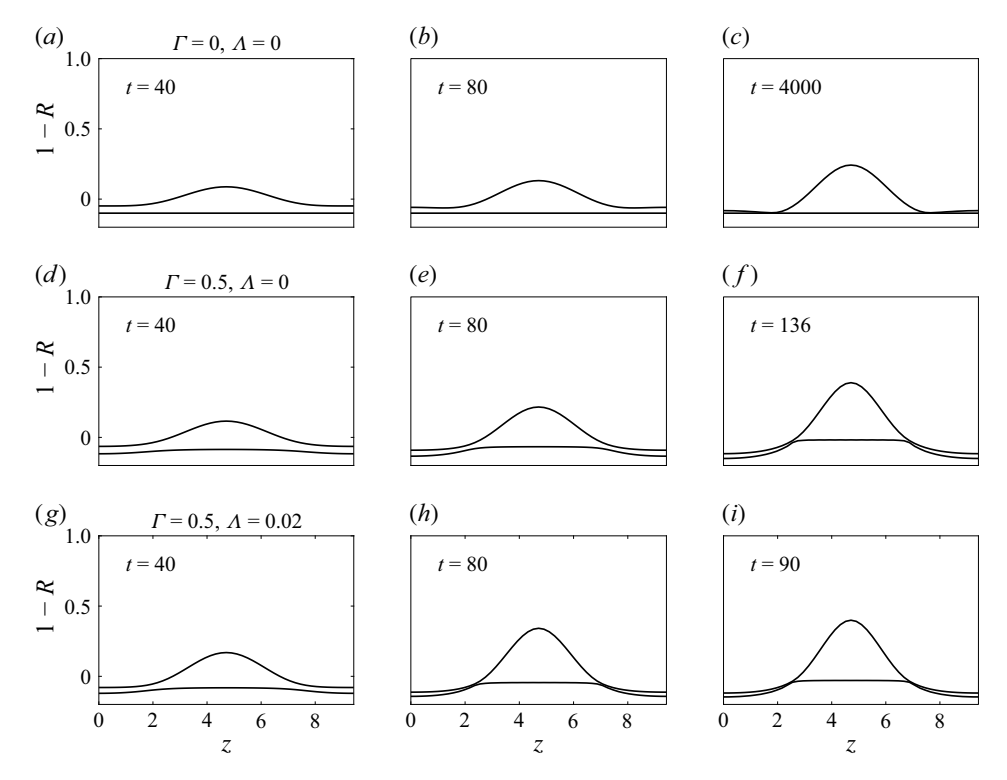


Figure 6. (a)–(c) Snapshots of the free-surface profile and tube wall corresponding to the  $\Gamma=0$ ,  $\Lambda=0$  case from figure 5. (d)–(f) Snapshots corresponding to the  $\Gamma=0.5$ ,  $\Lambda=0$  case. (g)–(i) Snapshots corresponding to the  $\Gamma=0.5$ ,  $\Lambda=0.02$  case.

time occurs when both slip and flexibility are present, but the relative impact of these two traits depends on the film thickness.

## 4.3. Base flow

The case of base flow due to gravity is examined next. In the case of a rigid tube, it has been shown that base flow due to gravity, although not contributing to linear instability, provides a nonlinearly stabilising force that inhibits plug formation and increases the critical thickness required for plug formation (Dietze *et al.* 2020; Ogrosky, 2021*a*; Camassa, Ogrosky & Olander 2024). How do tube flexibility and slip impact the evolution of falling films?

Simulations for a variety of parameter value combinations were run; the 'standard' case parameter values used throughout this section are shown in table 2. Figure 8(a) shows a waterfall plot of the free surface with these values; as it turns out, these values correspond to a critical thickness very near  $a_0 = 1.12$ . The film settles into a series of waves which fall down the tube; wave coalescence occurs between several of the waves, with the largest of the waves eventually becoming large enough that during a wave merger,  $R \to 0$  in finite time, indicating the formation of a plug.

How does each parameter – such as  $\Gamma$ ,  $\psi$ ,  $\Lambda$  and  $T_l$  – impact whether plugs form, and the time until a plug is formed? Model solutions were found for the standard case in table 2, as well as cases in which a single parameter value is changed from those standard values. Figure 9 shows the evolution of  $\min_z R(z, t)$  and  $\min_z a(z, t)$  for each case with a domain length of  $4\pi$ , which is of sufficient width to produce a single wave in each case. Identical initial conditions were used in each simulation.

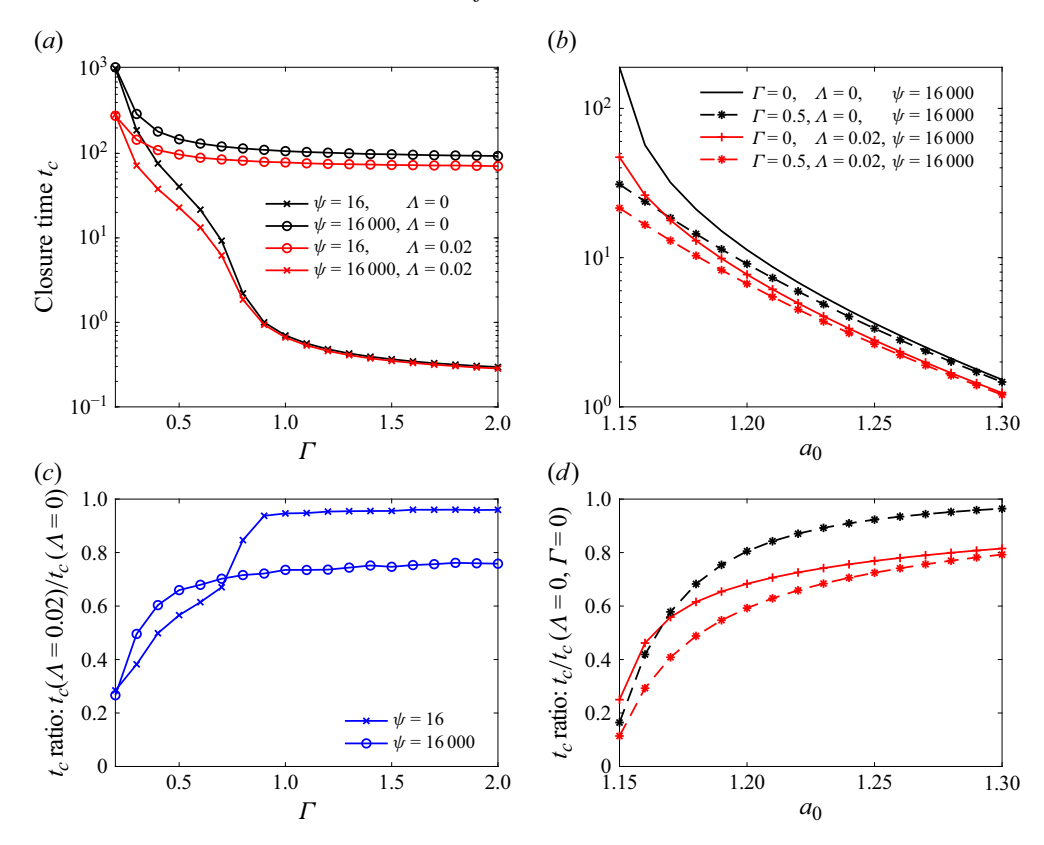


Figure 7. (a) Closure time  $t_c$  as a function of  $\Gamma$  for various  $\psi$  and  $\Lambda$ ;  $a_0 = 1.1$ ,  $Ca^{(g)} = Bo = T_l = T_0 = 0$ . (b) Closure time as a function of  $a_0$  for various  $\Gamma$ ,  $\psi$  and  $\Lambda$ ;  $Ca^{(g)} = Bo = T_l = T_0 = 0$ . (c) Ratio of closure time with slip to closure time without slip for two values of  $\psi$  as a function of  $\Gamma$ ; marker symbols correspond to those in (a). (d) Ratio of closure time with slip and/or flexibility to closure time of rigid tube with no slip; marker symbols correspond to those in (b).

The only solution in which a plug did not form was the rigid tube ( $\Gamma = 0$ ) solution;  $a = a_0$  is a constant in this case, and  $\min_z R(z,t)$  approaches a fixed value. Of the flexible tube simulations, the standard case took the greatest amount of time to produce a plug; increasing  $T_l$  to one had little impact on the solution. Increasing  $\Gamma$  to one – past the value  $1/a_0^3$  – resulted in a plug forming faster due to the k=0 mode of the wall decreasing. Increasing slip reduces the plug formation time considerably, while resulting in the smallest wall deviations. Decreasing damping results in the greatest deviation of  $\min_z a(z,t)$  from  $a_0$ , and plugs form fastest in this case.

In order to assess the impact of varying each parameter on the critical thickness required for plug formation, simulations could be repeatedly run for each parameter value with a variety of film thicknesses known to be near the critical thickness; the critical thickness would then be in a range between the largest thickness for which plugs did not form and the smallest thickness for which plugs formed. Based on figure 9,  $a_0 = 1.15$  appears to be below the critical thickness for the rigid tube case, but above the critical thickness for all other cases considered here.

A second way to assess the impact each parameter has on this critical thickness is to examine turning points in families of travelling-wave solutions, as in, e.g. Camassa *et al.* (2014), Ding *et al.* (2019), Dietze *et al.* (2020) and Dietze (2024). Figure 10 shows

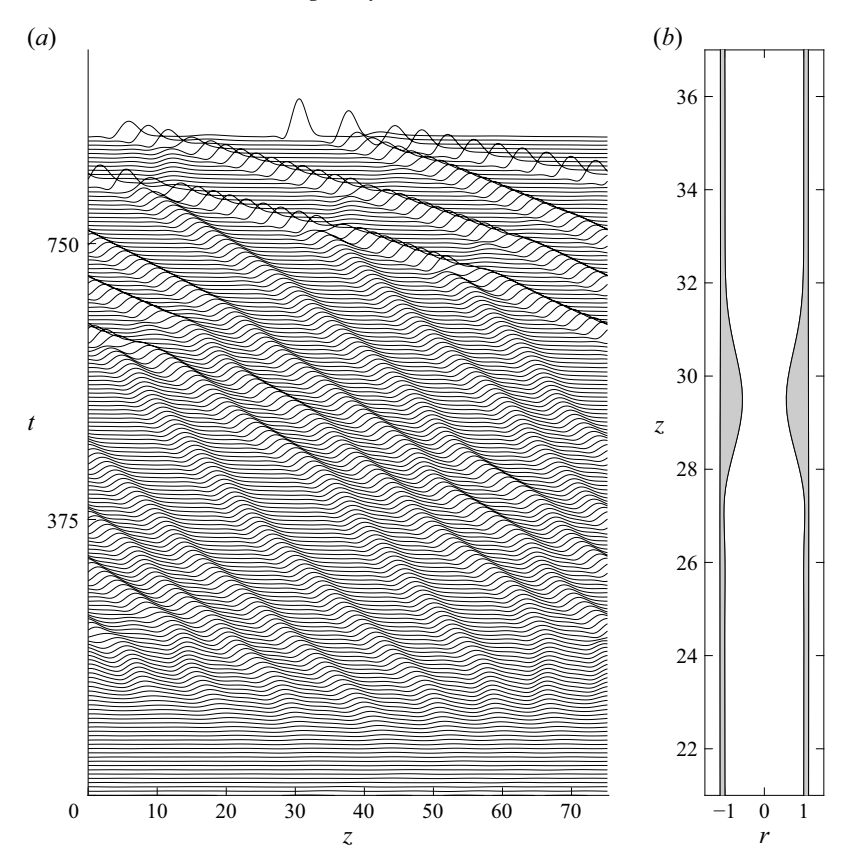


Figure 8. (a) Time snapshots of  $h = a_0 - R$  in a solution to model equations (2.16) and (2.19) with domain length  $L = 24\pi$  and with standard base flow parameter values in table 2; gravity acts right to left. Snapshots shown every  $\Delta t \approx 7.2$  in a frame of reference moving with the linearly most unstable wavenumber. (b) Snapshot in a tube corresponding to final snapshot in (a), zoomed in around largest wave; plug forms prior to next snapshot.

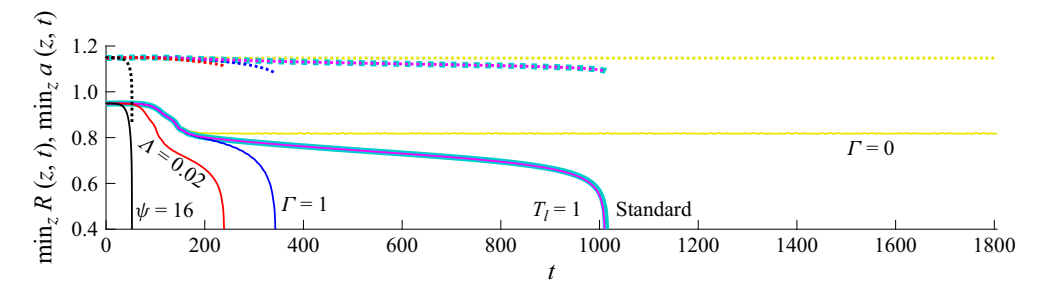


Figure 9. Evolution of  $\min_z R(z, t)$  and  $\min_z a(z, t)$  for simulations with base flow and domain  $L = 4\pi$ . Standard case (thick cyan line) refers to values in table 2. All other cases have identical parameter values except those indicated by text labels.

families of travelling-wave solutions for each of the cases shown in figure 9 (except  $\Gamma = 1$ ) as a function of  $a_0$ . Each point on a solid curve represents a travelling-wave solution with  $\min_Z R(Z)$ ; the corresponding value of  $\min_Z a(Z)$  lies on the corresponding dashed curve. Each family contains a turning point at some value of  $a_0$ , in which a lower branch and upper branch merge. Upper branch solutions in the rigid tube case are unstable with

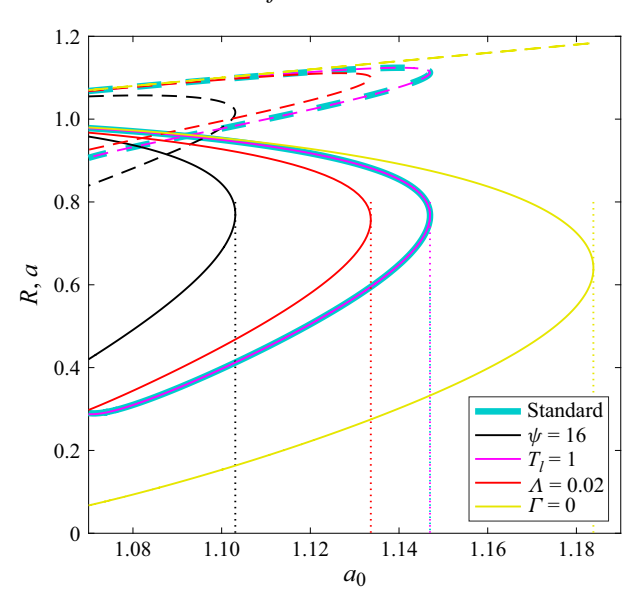


Figure 10. Travelling-wave solution families with period  $L = 4\pi$ . Standard case (thick cyan line) refers to values in table 2. All other cases have identical parameter values except those indicated by text labels. Colours correspond to parameter values in figure 9.

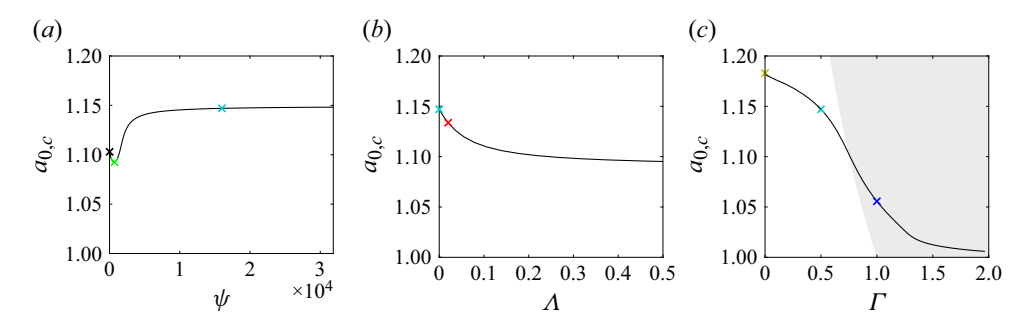


Figure 11. Turning-point thickness dependence on (a)  $\psi$ , (b)  $\Lambda$  and (c)  $\Gamma$ . All other parameter values correspond to the standard case in table 2. The  $\times$  symbols denote parameter values in figure 9. (c) Shading denotes region where  $\Gamma > 1/a_0^2$ .

a single large positive real eigenvalue (Camassa *et al.* 2016); waves with these amplitudes in all cases are never seen in solutions to the evolution equations, and are not explored further here. As has been shown in previous studies the value of  $a_{0,c}$  corresponding to each turning point provides a proxy for the critical thickness required for plugs to form. Note that  $a_0 = 1.15$  lies to the left of this turning-point thickness for the rigid tube, but to the right of all other cases, consistent with figure 9; it is only slightly to the right of the standard and  $T_l = 1$  cases, helping to explain the long time for plug formation to occur in those cases.

There is no deflection in the wall for the rigid tube case, as shown by the straight line for  $\min_Z a(Z)$  in the  $\Gamma=0$  case. The largest deflection again occurs for the small-damping case  $\psi=16$ . The amplitude of the turning-point wave is much less in all flexible tube cases than in the rigid tube case.

One benefit of this approach to identifying the critical thickness is that it is possible to explore the dependence of  $a_{0,c}$  on parameter values very quickly. Figure 11 shows this

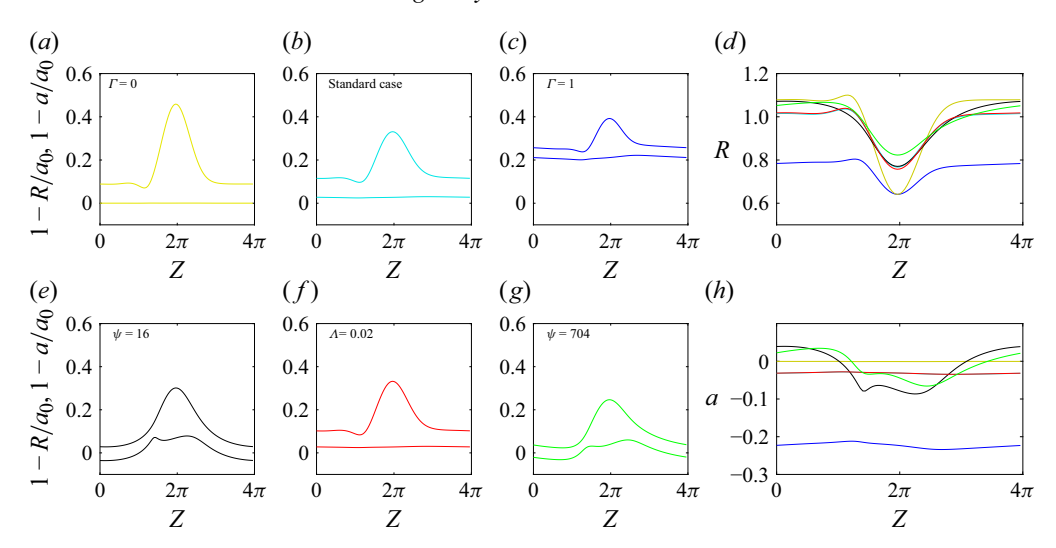


Figure 12. Travelling-wave solutions corresponding to  $\times$  symbols in figure 11.

dependence of  $a_{0,c}$  on  $\psi$ ,  $\Lambda$  and  $\Gamma$ . This proxy thickness  $a_{0,c}$  decreases with increasing slip  $(\Lambda)$  and increasing flexibility  $(\Gamma)$ . As was noted in Schwitzerlett *et al.* (2023), there appears to be a limiting value of  $a_{0,c} > 1$  as  $\Lambda$  gets arbitrarily large. The dependence of  $a_{0,c}$  on  $\psi$  is non-monotonic, with some minimal value for  $a_{0,c}$  obtained at finite  $\psi$  (roughly  $\psi \approx 44$  in figure 11a).

One caveat is that in the case of large  $\Gamma$ , in which  $\Gamma > 1/a_0^3$ , the travelling-wave solutions seen in figure 11(c) are not observed in solutions to the evolution equations. Instead, growth of the k=0 mode overtakes all other features, as described by Halpern & Grotberg (1992) for the 'compliant collapse' case. These turning points thus cannot necessarily be taken as a proxy for the critical thickness.

The waves corresponding to each turning point in figure 10 (also denoted by  $\times$  symbols in figure 11) are shown in figure 12. Note the shape of the wall profile in each case: the rigid tube case in (a) has no displacement, while the standard case (b) and slip case (f) show very little deviation from  $a_0$  other than a small k=0 perturbation. In the large  $\Gamma$  case, there is marked deviation in the k=0 mode of a, along with asymmetric displacement of a in the wave support region. In the small-damping case (e), the wall exhibits an asymmetric ripple in the wall at the leading edge of the wave; for moderate damping (g) a combination of the asymmetry seen in (c) and (e) is visible. The free surface in (a), (b), (c) and (f) displays a capillary ripple on the leading edge of the wave, as is typical in falling film flows. In (e) and (g), however, there is no such ripple visible in the free surface, although one is visible in the wall profile. The free surface (wall) profiles are plotted on top of one another in figures 12(d) and 12(h); the reduced amplitude (relative to the rigid tube case) is visible in all cases, and the k=0 mode deviations are apparent in (h).

How does the value of Bo impact  $a_{0,c}$  in a flexible tube? In a rigid tube, the presence of base flow due to gravity plays a nonlinearly stabilising role, suppressing plug formation and increasing  $a_{0,c}$ .

The impact of Bo on  $a_{0,c}$  in a flexible tube is explored in figure 13. As with the rigid tube case, increasing Bo results in larger  $a_{0,c}$ , inhibiting plug formation. In the case of strong damping ( $\psi = 16\,000$ ), the impact of increasing  $\Gamma$  has a moderate impact for small Bo ( $Bo \lesssim 0.02$  for  $\Gamma = 0.5$ ), perhaps the least impact for a 'transition' region  $0.02 \lesssim Bo \lesssim 0.2$  (for  $\Gamma = 0.5$ ) and the most significant impact for higher Bo ( $Bo \gtrsim 0.2$ ). For weak damping,

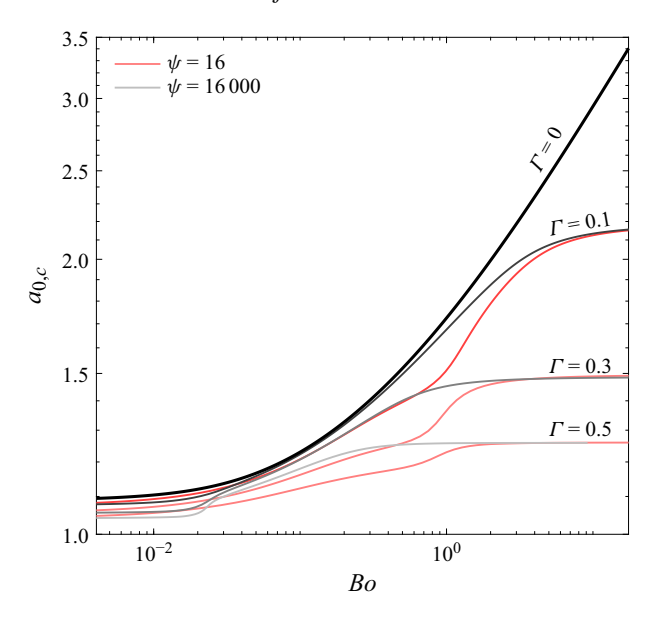


Figure 13. Turning-point thickness dependence on Bo for various values of  $\psi$  and  $\Gamma$ .

there still appears to be a similar type of transition region,  $0.6 \lesssim Bo \lesssim 2$ . For both small or large damping, the values of  $a_{0,c}$  are nearly identical in the case of either very small or very large Bo; to say the same thing another way, the damping has the most noticeable effect on  $a_{0,c}$  for intermediate values of Bo.

It was shown in Ogrosky (2021a) and Camassa et al. (2024) that the critical thickness can be made arbitrarily thick by increasing the value of Bo far enough. This is not the case for flexible tubes; there appears to be some  $a_{0,c,\infty}$  that  $a_{0,c}$  approaches as Bo gets arbitrarily large, with this thickness (horizontal asymptote) decreasing with  $\Gamma$ .

To summarise, figures 11 and 13 demonstrate the efficiency of this alternate way of identifying the critical thickness required for plug formation to occur. In the traditional approach, one would repeatedly run simulations for a single set of parameter values to sufficiently narrow down the region in which  $a_{0,c}$  lies. This would then need to be repeated, varying each parameter one at a time in small increments, to provide figures like figures 11 and 13. The alternate approach provides a shortcut; through numerical continuation of turning points, each of the curves in these plots can be found in a matter of seconds or minutes.

One caveat, however, is that all of the simulations above were conducted with a domain of  $L = 4\pi$ . How accurate is the critical thickness identified by turning points in predicting plug formation in larger domains, in which plugs may not only form through uninhibited growth of a single wave, but also through the merger of two waves?

Figure 14 shows the values of  $\min_z R(z, t)$  and  $\min_z a(z, t)$  for the same cases as in figure 9, but with domain length  $L = 24\pi$  and thickness  $a_0 = 1.12$ . Each simulation again began with identical initial conditions. In the rigid tube case ( $\Gamma = 0$ ), plugs were not seen to form in the simulation, with wave growth saturating and wave trains progressing down the tube.

On the other extreme, the case of decreasing damping ( $\psi = 1$ ) provides the only case in which a plug formed through growth of an individual wave, rather than through wave mergers. For the remaining cases, wave mergers occur in the simulation, with most mergers marked by a sharp drop in  $\min_z R(z, t)$ , followed by a slow partial rebounding

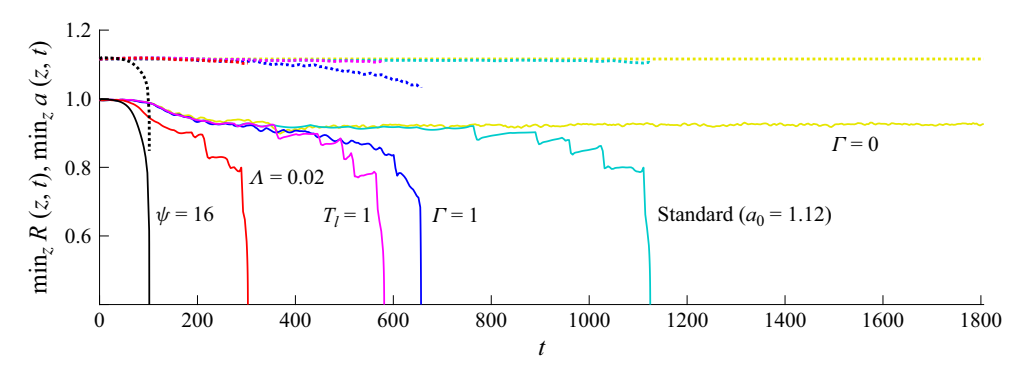


Figure 14. Evolution of  $\min_z R(z, t)$  and  $\min_z a(z, t)$  for simulations with base flow. Standard case (cyan) parameters are those of table 2 except that  $a_0 = 1.12$ ; domain length  $L = 24\pi$ . Other cases have all parameters identical to the standard case, with the exception of  $a_0 = 1.12$  and the parameter value indicated by the text.

of  $\min_z R(z, t)$  to some new quasi-steady value (seen most clearly in the first few mergers in the standard case). But for all cases except the rigid tube and small-damping case, a plug eventually formed through the coalescence of two waves, with the standard case taking the longest amount of time for a plug to form. This possibility of plug formation through wave mergers in longer tubes results in a decrease in the film thickness required for plugs to form.

For both the  $\psi=16$  and  $\Gamma=1$  cases, the tube wall pinched in noticeably (i.e.  $\min_z a(z,t)$  decreased noticeably prior to plug formation), demonstrating how increased flexibility and decreased damping promote the Plateau–Rayleigh instability through tube constriction. Increasing slip ( $\Lambda=0.02$ ) and longitudinal tension ( $T_l=1$ ) also promoted faster plug formation than the standard case, with slip noticeably promoting growth in the waves at early times, consistent with the increased growth rates that slip produces; in both these cases, wall deformations remained minimal.

It is interesting to note that the standard and  $T_l = 1$  cases are virtually identical until  $t \approx 375$ , at which point a wave merger occurs in the  $T_l = 1$  case, but does not for the standard case. Note that the  $T_l$  case leads to significantly shorter closure time than the standard case, in contrast to the  $L = 4\pi$  simulations. Also note that the  $\Gamma = 1$  case again corresponds to a case of 'compliant collapse' in the tube wall, seen by the significantly reduced value of  $\min_{z} a(z, t)$ .

Before concluding, we briefly explore the case of core-driven film flow in which  $Ca^{(g)} > 0$ . Much of the dynamics is similar to that of Bo > 0: long-wave growth saturates in a series of waves which interact and propagate in the direction of  $Q^{(g)}$ . One notable difference: in the 'locally Poiseuille' model used here plug formation does not occur in simulations due to the assumed constant volume flux  $Q^{(g)}$  and assumed large viscosity gradient in the model derivation.

How do tube flexibility and slip impact the transport of the film along the tube? The volume flux

$$Q(z,t) = 2\pi \left[ Ca^{(g)} f_1(R;a) + \frac{1}{16} \left( Bo R^2 + R_z + R^2 R_{zzz} \right) f_2(R,a) \right], \tag{4.3}$$

may be averaged over the domain

$$\tilde{Q}(t) = \frac{1}{L} \int_0^L Q(z, t) dz. \tag{4.4}$$

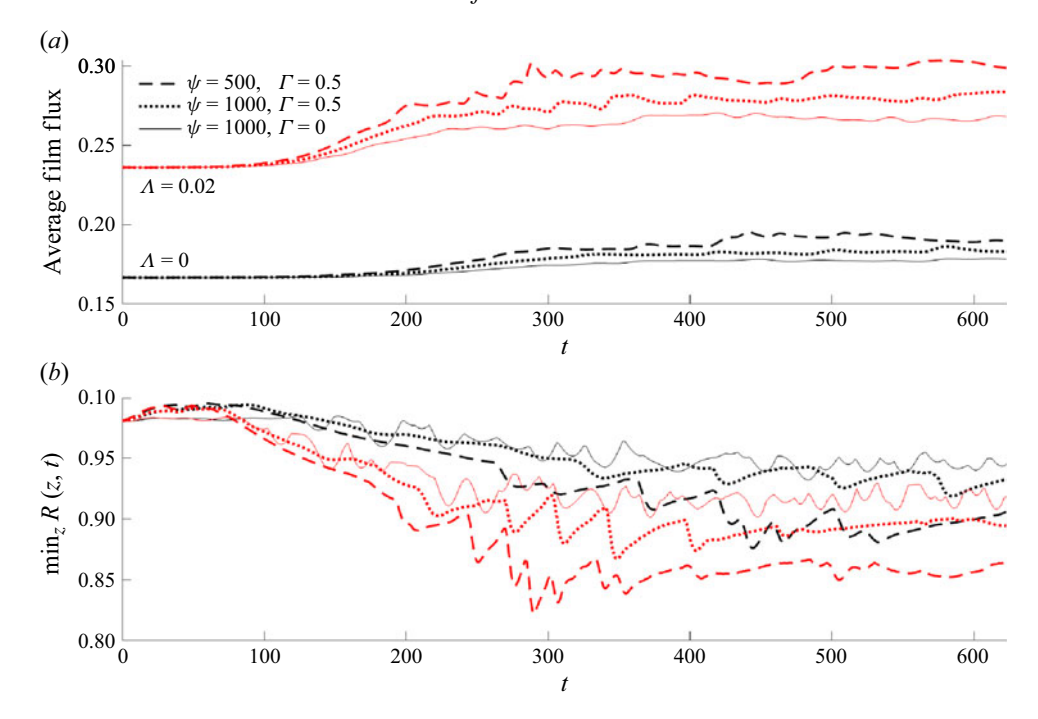


Figure 15. Evolution of (a) average volume flux  $\tilde{Q}(z,t) = (1/L) \int_0^L Q(z,t) dz$  and (b)  $\min_z R(z,t)$  for simulations with base flow due to core flow; domain length  $L = 24\pi$ ,  $Ca^{(g)} = 0.00625$ ,  $a_0 = 1.1$ ,  $Bo = T_l = T_0 = 0$ .

		$\Lambda = 0$	$\Lambda = 0.02$
$\Gamma = 0$		6.7 %	12.8 %
$\Gamma = 0.5$	$\psi = 1000$	10.3 %	18.8 %
$\Gamma = 0.5$	$\psi = 500$	15.0 %	27.4 %

Table 3. Per cent increase in film flux  $\tilde{Q}$  from beginning to end of simulation, calculated by dividing the mean of  $\tilde{Q}$  from t = 500 to t = 623 by the mean of  $\tilde{Q}$  from t = 0 to t = 50 in figure 15 and subtracting 1.

Figure 15(a) shows Q(t) for six simulations with various combinations of  $\Gamma$ ,  $\psi$  and  $\Lambda$ ; figure 15(b) shows the value of  $\min_z R(z, t)$ . In each case, much of the film transport comes from the leading-order velocity profile corresponding to perfect core–annular flow with a constant free surface; the value of this leading-order flux can be seen in the initial period of the simulation ( $t \lesssim 100$ ). Slip plays a large role in promoting film transport as can be expected due to its impact on this leading-order velocity profile.

In all cases, the growth of waves also contributes to the flux, enhancing film transport. While tube flexibility does not impact the leading-order velocity, it does enhance film transport through larger wave growth and higher-amplitude waves. Table 3 shows the percent increase in film transport over the duration of each simulation in figure 15, calculated by averaging  $\tilde{Q}$  from t = 500 to the end of the simulation, dividing this by the mean of  $\tilde{Q}$  from t = 0 to t = 50, and subtracting 1.

## 5. Conclusions

Viscous film flow inside a slippery, flexible tube has been studied via a two-equation long-wave asymptotic model derived here. The model is valid for moderately thick films, and accounts for tube flexibility, wall damping, longitudinal tension, slip length and strength of base flow due either to gravity or airflow.

Linear stability analysis of the model shows that, in the absence of base flow, there is one unstable mode, and that there is a critical value of  $\Gamma=1/a_0^3$ ; above this value, the tube has a combined Plateau–Rayleigh/elastic instability for the k=0 mode which can trigger compliant collapse due to the tube's flexibility. Growth rates increase with flexibility and slip, and decrease with damping and tension. In the presence of base flow, it is possible for two unstable modes to exist; increasing the strength of the base flow reduces the maximum growth rate in all cases explored here.

Numerical solutions of the nonlinear evolution equations were used to study plug formation (and time to closure). In the absence of base flow, slip was found to have a pronounced impact on closure time (decreasing it up to a factor of 4) in tubes with small-to-moderate flexibility and strong damping; wall deformations were reduced when slip was present. For more flexible or weakly damped tubes, the elastic instability drove the evolution, and slip had little impact on closure time. For falling films, the critical thickness required for plugs to form was shown to decrease with slip, flexibility and tension. The impact of damping was non-monotonic, with some finite  $\psi$  producing the smallest critical thickness over all values. For flexible tubes, given a fixed value of  $\Gamma$ , there is a largest critical thickness that cannot be exceeded regardless of strength of base flow; this is in contrast to the rigid tube case, in which the critical thickness may be made arbitrarily large by sufficiently increasing the strength of the base flow. For air-driven films, both slip and flexibility were shown to increase the rate of film transport along the tube.

One benefit of the travelling-wave approach used here to identify the critical thickness is its efficiency when studying large regions of parameter space.

The model was derived under a number of simplifying assumptions which may not be valid in all physical applications. The model assumed axisymmetric flow; non-axisymmetric flow and wall deformations are likely significant, particularly in the case of compliant collapse. Only radial deformations of the wall were included; axial deflections may be important in some applications.

Funding. This work was supported by the Simons Foundation, no. 854116.

**Declaration of interests.** The authors report no conflict of interest.

#### REFERENCES

BÄUMCHEN, O. & JACOBS, K. 2009 Slip effects in polymer thin films. J. Phys.: Condens. Matter 22, 033102–1–21.

BILEK, A.M., DEE, K.C. & GAVER, D.P.III 2003 Mechanisms of surface-tension-induced epithelial cell damage in a model of pulmonary airway reopening. *J. Appl. Physiol.* **94**, 770.

BROCHARD-WYART, F., DE GENNES, P.-G., HERVERT, H. & REDON, C. 1994 Wetting and slippage of polymer melts on semi-ideal surfaces. *Langmuir* 10, 1566–1572.

CAMASSA, R., FOREST, M.G., LEE, L., OGROSKY, H.R. & OLANDER, J. 2012 Ring waves as a mass transport mechanism in air-driven core-annular flows. *Phys. Rev. E* 86, 066305.

CAMASSA, R., MARZUOLA, J., OGROSKY, H.R. & VAUGHN, N. 2016 Traveling waves for a model of gravity-driven film flows in cylindrical domains. *Physica D* 333, 254–265.

CAMASSA, R., OGROSKY, H.R. & OLANDER, J. 2014 Viscous film flow coating the interior of a vertical tube. Part I. Gravity-driven flow. *J. Fluid Mech.* **745**, 682–715.

CAMASSA, R., OGROSKY, H.R. & OLANDER, J. 2024 A long-wave model for a falling upper convected Maxwell film inside a tube. *J. Fluid Mech.* **1001**, A14-1–A14-28.

- CASSIDY, K.J., HALPERN, D., RESSLER, B.G. & GROTBERG, J.B. 1999 Surfactant effects in model airway closure experiments. *J. Appl. Physiol.* **87**, 415–427.
- Craster, R.V. & Matar, O.K. 2009 Dynamics and stability of thin liquid films. *Rev. Mod. Phys.* 81 (3), 1131.
- DIETZE, G.F. & RUYER-QUIL, C. 2015 Films in narrow tubes. J. Fluid Mech. 762, 68-109.
- DIETZE, G., LAVALLE, G. & RUYER-QUIL, C. 2020 Falling liquid films in narrow tubes: occlusion scenarios. J. Fluid Mech. 894, A17.
- DIETZE, G. 2024 Liquid plugs in narrow tubes: application to airway occlusion. *J. Fluid Mech.* **998**, A50–1–43.
- DING, Z., LIU, Z., LIU, R. & YANG, C. 2019 Thermocapillary effect on the dynamics of liquid films coating the interior surface of a tube. *Intl J. Heat Mass Transfer* **138**, 524–533.
- DOEDEL, E.J., CHAMPNEYS, A.R., DERCOLE, F., FAIRGRIEVE, T., KUZNETSOV, Y., OLDEMAN, B., PAFFENROTH, R., SANDSTEDE, B.J., WANG, X. & ZHANG, C. 2008 AUTO-07P: Continuation and Bifurcation Software for Ordinary Differential Equations. Montreal Concordia University.
- ELAD, D., FOUX, A. & KIVITY, Y. 1988 A model for the nonlinear elastic response of large arteries. *J. Biomed. Engng.* 110, 185–189.
- ELAD, D., KAMM, R.D. & SHAPIRO, A.H. 1988 Tube law for the intrapulmonary airway. J. Appl. Physiol. 110, 185–189.
- ERMENTROUT, B. 2002 Simulating, Analyzing, and Animating Dynamical Systems. SIAM.
- FRENKEL, A.L. 1992 Nonlinear theory of strongly undulating thin films flowing down vertical cylinders. *Europhys. Lett.* **18**, 583–588.
- FUJIOKA, H., HALPERN, D., RYANS, J. & GAVER, D.P. 2016 Reduced-dimension model of liquid plug propagation in tubes. *Phys. Rev. Fluids* 1, 053201.
- GAUGLITZ, P. & RADKE, C. 1988 An extended evolution equation for liquid film breakup in cylindrical capillaries. Chem. Engng Sci. 43 (7), 1457–1465.
- GOREN, S.L. 1962 The instability of an annular thread of fluid. J. Fluid Mech. 12 (2), 309-319.
- GROTBERG, J.B. & JENSEN, O.E. 2004 Biofluid mechanics in flexible tubes. *Annu. Rev. Fluid Mech.*. **36**, 121–147.
- HAEFNER, S., BENZAQUEN, M., BAUMCHEN, O., SALEZ, T., PETERS, R., MCGRAW, J.D., JACOBS, K., RAPHAEL, E. & DALNOKI-VERESS, K. 2015 Influence of slip on the Plateau–Rayleigh instability on a fibre. Nat. Commun. 6 (1), 1–6.
- HALPERN, D. & GROTBERG, J.B. 1992 Fluid-elastic instabilities of liquid-lined flexible tubes. J. Fluid Mech. 244, 615–632.
- HALPERN, D. & GROTBERG, J.B. 1993 Surfactant effects on fluid-elastic instabilities of liquid-lined flexible tubes: a model of airway closure. J. Biomech. Engng 115, 271–277.
- HALPERN, D., JENSEN, O.E. & GROTBERG, J.B. 1998 A theoretical study of surfactant and liquid delivery into the lung. J. Appl. Physiol. 85 (1), 333–352.
- HALPERN, D. & WEI, H.-H. 2017 Slip-enhanced drop formation in a liquid falling down a vertical fibre. *J. Fluid Mech.* **820**, 42–60.
- HAMMOND, P. 1983 Nonlinear adjustment of a thin annular film of viscous fluid surrounding a thread of another within a circular cylindrical pipe. *J. Fluid Mech.* **137**, 363–384.
- HEIL, M. 1999 Airway closure: occluding liquid bridges in strongly buckled elastic tubes. J. Biomech. Engng 121, 487–493.
- HEIL, M., HAZEL, A.L. & SMITH, J.A. 2008 The mechanics of airway closure. *Respir. Physiol. Neurobiol.* 163, 214–221.
- HICKOX, C.E. 1971 Instability due to viscosity and density stratification in axisymmetric pipe flow. *Phys. Fluids* 14 (2), 251–262.
- HILL, D.B., BUTTON, B., RUBINSTEIN, M. & BOUCHER, R. 2022 Physiology and pathophysiology of human airway mucus. *Physiol. Rev.* **102**, 1757–1836.
- HOSSAIN, M.M. & BEHERA, H. 2022 Shear-imposed falling thin Newtonian film over a porous slippery surface. *Phys. Fluids* **34**, 114124.
- HOWELL, P.D., ROBINSON, J. & STONE, H.A. 2013 Gravity-driven thin-film flow on a flexible substrate. J. Fluid Mech. 732, 190–213.
- JENSEN, O.E. 2000 Draining collars and lenses in liquid-lined vertical tubes. *J. Colloid Interface Sci.* **221**, 38–49.
- JI, H., FALCON, C., SADEGHPOUR, A., ZENG, Z., JU, Y.S. & BERTOZZI, A.L. 2019 Dynamics of thin liquid films on vertical cylindrical fibres. J. Fluid Mech. 865, 303–327.
- JOSEPH, D.D., BAI, R., CHEN, K. & RENARDY, Y.Y. 1997 Core-annular flows. Annu. Rev. Fluid Mech. 29 (1), 65–90.

# H.R. Ogrosky and M. Schwitzerlett

- KALLIADASIS, S. & CHANG, H.-C. 1994 Drop formation during coating of vertical fibres. *J. Fluid Mech.* **261**, 135–168.
- KAVOKINE, N., NETZ, R.R. & BOCQUET, L. 2021 Fluids at the nanoscale: from continuum to subcontinuum transport. Annu. Rev. Fluid Mech. 53, 377–410.
- KERCHMAN, V. & FRENKEL, A. 1994 Interactions of coherent structures in a film flow: simulations of a highly nonlinear evolution equation. *Theor. Comput. Fluid Dyn.* 6 (4), 235–254.
- KERCHMAN, V. 1995 Strongly nonlinear interfacial dynamics in core–annular flows. J. Fluid Mech. 290, 131–166.
- KIM, C.S., RODRIGUEZ, C.R., ELDRIDGE, M.A. & SACKNER, M.A. 1986 Criteria for mucus transport in the airways by two-phase gas-liquid flow mechanism. *J. Appl. Physiol.* **60**, 901–907.
- KIM, C.S., GREENE, M.A., SANKARAN, S. & SACKNER, M.A. 1986 Mucus transport in the airways by two-phase gas-liquid flow mechanism: continuous flow model. *J. Appl. Physiol.* **60**, 908–917.
- KIM, C.S., IGLESIAS, A.J. & SACKNER, M.A. 1987 Mucus clearance by two-phase gas-liquid flow mechanism: asymmetric periodic flow model. J. Appl. Physiol. 62, 959–971.
- LAUGA, E., BRENNER, M.P. & STONE, H.A. 2005 Microfluidics: the no-slip boundary condition. In *Springer Handbook of Experimental Fluid Mechanics* (eds. C. TROPEA, A.L. YARIN & J.F. FOSS), Springer Handbooks. Springer.
- LIU, R. & DING, Z. 2017 Stability of viscous film flow coating the interior of a vertical tube with a porous wall. *Phys. Rev. E* **95**, 053101.
- MAGHSOUDI-GANJEH, M., SATTARI, S. & ESKANDARI, M. 2021 Mechanical behavior of the airway wall in respiratory disease. *Curr. Opin. Physiol.* 22, 100445–1–6.
- OGROSKY, H.R. 2021a Linear stability and nonlinear dynamics in a long-wave model of film flows inside a tube in the presence of surfactant. *J. Fluid Mech.* **908**, A23.
- OGROSKY, H.R. 2021b Impact of viscosity ratio on falling two-layer viscous film flow inside a tube. *Phys. Rev. Fluids* 6, 104005–1–27.
- ORON, A., DAVIS, S.H. & BANKOFF, S.G. 1997 Long-scale evolution of thin liquid films. *Rev. Mod. Phys.* 69 (3), 931.
- PATNE, R. 2021 Purely elastic instabilities in the airways and oral area. J. Fluid Mech. 928, A22-1-32.
- QUEVEDO TIZNADO, Q.A., FUENTES, C., GONZÁLEZ-SOSA, E. & CHÁVEZ, C. 2018 Snap-off criteria for dynamic flow conditions in constricted circular capillaries. *J. Appl. Fluid Mech.* 11, 447–457.
- RYANS, J., FUJIOKA, H., HALPERN, D. & GAVER, D.P. 2016 Reduced-dimension modeling approach for simulating recruitment/De-recruitment dynamics in the lung. *Ann. Biomed. Engng* 44, 3619–3631.
- SAMANTA, A., RUYER-QUIL, C. & GOYEAU, B. 2011 A falling film down a slippery inclined plane. *J. Fluid Mech.* **684**, 353–383.
- SAMANTA, A., GOYEAU, B. & RUYER-QUIL, C. 2013 A falling film on a porous medium. J. Fluid Mech. 716, 414–444.
- SCHWITZERLETT, M., OGROSKY, H.R. & TOPALOGLU, I. 2023 A long-wave model for film flow inside a tube with slip. *J. Fluid Mech.* **974**, A22–1–28.
- WHANG, J., FAULMAN, C., ITIN, T.A. & GAVER, D.P. 2017 The influence of tethering and gravity on the stability of compliant liquid-lined airways. *J. Biomech.* **50**, 228–233.
- YIH, C.-S. 1967 Instability due to viscosity stratification. J. Fluid Mech. 27 (2), 337–352.
- ZHOU, Z.-Q., PENG, J., ZHANG, Y.-J. & ZHUGE, W.-L. 2014 Instabilities of viscoelastic liquid film coating tube in the presence of surfactant. *J. Non-Newtonian Fluid Mech.* **204**, 94–103.
- ZHOU, Z.-Q., PENG, J., ZHANG, Y.-J. & ZHUGE, W.-L. 2016 Viscoelastic liquid film flowing down a flexible tube. *J. Fluid Mech.* **802**, 583–610.